Journal of Quantitative Spectroscopy & Radiative Transfer 210 (2018) 1–18

Contents lists available at ScienceDirect

Journal of Quantitative Spectroscopy & Radiative Transfer

journal homepage: www.elsevier.com/locate/jqsrt

High-temperature partition functions, specific heats and spectral radiative properties of diatomic molecules with an improved calculation of energy levels

Z. Qin[a], J.M. Zhao[a], L.H. Liu[a,b,*]

[a] School of Energy Science and Engineering, Harbin Institute of Technology, Harbin 150001, China
[b] School of Energy and Power Engineering, Shandong University, Qingdao 266237, China

ARTICLE INFO

Article history:
Received 26 January 2018
Revised 5 February 2018
Accepted 5 February 2018
Available online 6 February 2018

Keywords:
Diatomic molecules
Non-equilibrium
Partition function
Thermodynamic properties
Spectral radiative properties

ABSTRACT

The level energies of diatomic molecules calculated by the frequently used Dunham expansion will become less accurate for high-lying vibrational and rotational levels. In this paper, the potential curves for the lower-lying electronic states with accurate spectroscopic constants are reconstructed using the Rydberg–Klein–Rees (RKR) method, which are extrapolated to the dissociation limits by fitting of the theoretical potentials, and the rest of the potential curves are obtained from the ab-initio results in the literature. Solving the rotational dependence of the radial Schrödinger equation over the obtained potential curves, we determine the rovibrational level energies, which are then used to calculate the equilibrium and non-equilibrium thermodynamic properties of N_2, N_2^+, NO, O_2, CN, C_2, CO and CO^+. The partition functions and the specific heats are systematically validated by available data in the literature. Finally, we calculate the radiative source strengths of diatomic molecules in thermodynamic equilibrium, which agree well with the available values in the literature. The spectral radiative intensities for some diatomic molecules in thermodynamic non-equilibrium are calculated and validated by available experimental data.

1. Introduction

The partition functions are key to the calculation of the energy level populations of high-temperature gases produced in Earth and Mars atmospheric entry [1,2]. And the energy level populations are input parameters in the calculation of the spectral radiative properties of high-temperature gases in equilibrium and local non-equilibrium systems [1]. The obtained spectral radiative properties can be used to predict the atmospheric radiative transfer [3] and the radiative heat flux of aircraft surface caused by shock waves in atmospheric entries [4]. Moreover, the partition functions can also be used to calculate the thermodynamic properties, which are required in the calculation of the aerothermodynamic flow field [5–8].

Strong shock waves can be formed in front of the vehicles during hypersonic flights, which translate part of the kinetic energy of the vehicles into the internal energy of gases. As a result, the gas temperature rises precipitously, leading to the non-equilibrium between the vibrational and rotational modes for molecular components. However, the excitation of different energy modes will not occur at the same time, making it difficult to adopt a single temperature to accurately describe the thermal non-equilibrium phenomenon among different energy modes. To simplify the problem, Lee [9] and Park [10] assumed that various energy modes can be separated by the corresponding temperatures, known as the multi-temperature model. For instance, the frequently used two-temperature model uses T_r to represent the temperature of the rotational and translational energy levels with a Boltzmann and Maxwell distribution, and uses T_v to represent the temperature of the electronic and vibrational energy levels with Boltzmann distributions (shown in Fig. 1). Recently, the state-to-state model becomes more and more popular due to the availability of the ever-increasing ab-initio rate parameters for the elementary collisional processes. It was shown that the state-to-state model can predict better the number densities of the species in high-temperature non-equilibrium reacting flows [11–13], in which different vibrational temperatures are introduced for each corresponding molecule and even for each electronic state of the same molecule. For these two non-equilibrium models, the thermodynamic and spectral radiative properties of high-temperature gases cannot be described using one temperature. Instead, the rovibrational interaction energy should be divided into multiple parts with the cor-

* Corresponding author.
E-mail addresses: lhliu@hit.edu.cn, liulinhua@sdu.edu.cn (L.H. Liu).

https://doi.org/10.1016/j.jqsrt.2018.02.004
0022-4073/

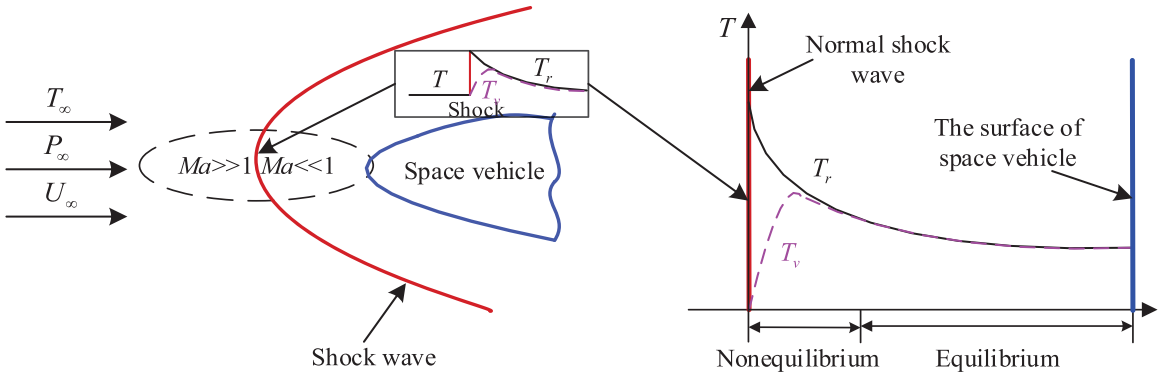

Fig. 1. Schematic diagram of thermodynamic parameters behind a shock in hypersonic flow (T_∞, P_∞, U_∞ are respectively the temperature, pressure and velocity before the shock, T_r, T_v are respectively the translational and vibrational temperature, Ma is the Mach number).

responding temperatures. Hence, Jaffe et al. [5] proposed the two limiting cases to split the rovibrational internal energy based on the two-temperature model. This method is the starting point to resolve the non-equilibrium thermodynamic and spectral radiative properties, which can also be generalized to the multi-temperature and state-to-state models if the summation over each internal energy mode is performed for its own temperature.

As required in the study of the plasma flow for atmospheric entry, a large amount of data of the partition functions, the thermodynamic and spectral radiative properties for high-temperature gases have been calculated over the past few years. For the partition functions and thermodynamic properties, Drellishak et al. [14,15] calculated the equilibrium chemical composition and the thermodynamic properties of argon, nitrogen and oxygen plasma for temperatures as high as 35000 K. In order to derive the entropy and enthalpy of gas mixtures for the calculation of non-equilibrium flow field, Jaffe [5] proposed a scheme for partitioning the internal energy into vibrational, rotational and electronic parts, in which two extreme cases of splitting the rovibrational interaction energy are considered. With the aid of this scheme, the two-temperature energies of N_2, O_2 and NO were found to be insensitive to the two extreme cases [5]. Employing the two-temperature partitioning scheme, Babou et al. [2] calculated the two-temperature internal partition functions, internal energies, vibrational and rotational specific heats of N_2, N_2^+, NO, O_2, CN, C_2, CO and CO^+ from 1000 to 50000 K. McBride et al. [16] reported a library of thermodynamic data of more than 2000 individual species, from which the equilibrium thermodynamic properties ranging from 200 to 20000 K can be found for the gaseous chemical species related to planetary atmosphere. Capitelli et al. [7] presented the thermodynamic properties of the components related to the Martian atmosphere. In addition, a spectroscopic database is built by the EM2C laboratory in France [1] for radiative transfer calculations in air and CO_2–N_2 plasmas.

Notice that all the rovibrational level energies for the bound and quasi-bound electronic states of diatomic molecules in previous published papers are calculated based on the Dunham expansion, which is given by [17]

$$E_{n,v,J} = hc \sum_{i=0,j=0} Y_{ij}\left(v+\frac{1}{2}\right)^i [J(J+1)]^j \tag{1}$$

where Y_{ij} is the Dunham coefficients. For j=0, Eq. (1) reduces to the vibrational level energy, which is generally expressed as expansions of the anharmonic oscillator limit [17]

$$G_v = \sum_{i=0} Y_{i0}\left(v+\frac{1}{2}\right)^i = T_e + \omega_e\left(v+\frac{1}{2}\right) - \omega_e\chi_e\left(v+\frac{1}{2}\right)^2 + \omega_e y_e\left(v+\frac{1}{2}\right)^3 + \cdots \tag{2}$$

And the internal rotational constant for this vibrational level can be expanded as [17]

$$B_v = \sum_{i=0} Y_{i1}\left(v+\frac{1}{2}\right)^i = B_e - \alpha_e\left(v+\frac{1}{2}\right) + \gamma_e\left(v+\frac{1}{2}\right)^2 + \cdots \tag{3}$$

Moreover, analogous power series expansions in $(v+1/2)$ are used to express the v-dependence of the other rotational constants D_v (for j=2), H_v (for j=3), etc. [24]. It is simple and convenient to calculate the level energies by Dunham expansion. However, the Dunham coefficients in the literature are usually fitted by lower-lying levels due to the difficulty in measuring the higher-lying levels. Hence, the Dunham coefficients are only valid for the lower-lying rovibrational levels. Thus, the higher-lying rovibrational levels calculated by the fitted Dunham coefficients maybe diverge from the exact energies, which are very important in the calculation of the partition function at high temperatures.

Inspired by the work of da Silva et al. [18], we present a more precise calculation of the rovibrational level energies for all the electronic states of N_2, N_2^+, NO, O_2, CN, C_2, CO and CO^+ by resolving the rotational dependence of the radial Schrödinger equation over the accurate potential curves. And the potential curves are reconstructed by combining the well-known Rydberg–Klein–Rees (RKR) method [19–21] and ab-initio calculations [26,27]. Using the same cut-off criterion, the number of the vibrational and rotational levels predicted by this method is larger than those derived from the Dunham expansion. The increment of the level number is investigated due to its importance in the partition functions. After obtaining the rovibrational level energies, we calculate the equilibrium partition functions and thermodynamic properties of N_2, N_2^+, NO, O_2, CN, C_2, CO and CO^+. The non-equilibrium partition functions and thermodynamic properties of these molecules in the framework of the two-temperature model are also computed and studied considering the vibrational and rotational temperatures ranging from 1000 K to 50000 K. Moreover, the spectral radiative properties of diatomic molecules in air and CO_2–N_2 plasmas are investigated. This paper is organized as follows. In Section 2, we briefly describe the improved approach for the energy level calculation. The method to determine the maximum vibrational and rotational quantum number is also given. In Sections 3 and 4, the equilibrium and non-equilibrium thermodynamic properties are given and discussed. In Section 5, the spectral radiative properties of diatomic molecules required for radiative transfer calculations in air and CO_2–N_2 plasmas are investigated. In Section 6, conclusions are drawn.

2. The computational method

2.1. The internal partition function

According to the statistical mechanics [22,23], the internal partition function of any atom or molecule in thermodynamic equilibrium can be expressed by

$$Q_{\text{int}}(T) = \sum_i g_i exp\left(-\frac{\varepsilon_i - \varepsilon_0}{k_B T}\right) \tag{4}$$

where g_i and ε_i represent the degeneracy and the energy of the ith internal quantum level of the component under consideration, ε_0 refers to the energy of the lowest energy level, and k_B is the Boltzmann constant. For diatomic molecules, the treatment of the energy levels follows the method developed by Babou et al. [2], Jaffe [5], Capitelli et al. [7] and Herzberg [28], i.e., the energy of a specific state is split into three contributions: the electronic excitation energy $E_{el}(n)$, the vibrational energy $E_{vib}(n,v)$ and the rotational energy $E_{rot}(n,v,J)$ (Nuclear spin interactions are neglected in this paper). The electronic, vibrational and rotational energy levels of a diatomic molecule are strongly coupled, and the internal partition function can be given by

$$Q_{\text{int}}(T) = \sigma \sum_n^{n_{\max}} (2 - \delta_{\Lambda,0})(2S+1) \sum_v^{v_{\max}} \sum_J^{J_{\max}} (2J+1) \; exp\left(-hc\frac{E_{n,v,J} - \varepsilon_0}{k_B T}\right) \tag{5}$$

where n, v, J are the electronic, vibrational and rotational quantum numbers, respectively, the subscript max refers to the maximum allowable values of different internal quantum levels, h is the Planck's constant, c is the speed of light in vacuum, the degeneracy g_i in Eq. (4) includes the electronic degeneracy ($2\text{-}\delta_{\Lambda,0}$)($2S$+1), the rotational degeneracy ($2J$+1) and the symmetry factor σ (σ=1 for heteronuclear molecules and $\sigma = 1/2$ for homonuclear molecules), just as shown in Eq. (5), S is the total electronic spin angular momentum quantum number, Λ is the quantum number of the projection of the electronic orbital angular momentum on the internuclear axis, and $E_{n,v,J}$ is the energy of quantum state (n,v,J). As shown in Eq. (5), the energy $E_{n,v,J}$, the maximum vibrational and rotational quantum numbers v_{max} and J_{max} must be determined in order to obtain the internal partition function.

2.2. Improved approach for the calculation of level energies

Numerical approach of calculating the level energies by solving the radial Schrödinger equation over the accurate potential curve proves to be more accurate, as it tries its best to rebuild the overall potential curve to its dissociation limit. The potential curve can be reconstructed by quantum chemistry methods or quasi-classical methods. Quantum chemistry methods are usually called ab-initio methods since its calculations are directly from theoretical principles, just using a few basic physical constants, without regard to experimental and empirical parameters [31,32]. These methods are computationally intensive, and the accuracy of the calculated level energies is often lower than that of level energies obtained from quasi-classical methods for the electronic states where the level energies can be experimentally retrieved. da Silva et al. [18] pointed out that the spectroscopic accuracy in the determination of the level energies by quasi-classical methods can yield uncertainties as low as δE=10^{-3} cm^{-1}, which by far exceeds the possibilities of any ab-initio calculations. However, ab-initio methods can give credible and reliable results of higher-lying electronic states that are rarely obtained by experiments. Hence, for the higher-lying electronic states of diatomic molecules considered in this paper, the potential curves are derived from ab-initio results in the literature, which are given in Appendix A. The rest of the electronic potential curves are reconstructed by the Rydberg–Klein–Rees (RKR) [19–21] method, making use of the most up-to-date spectroscopic constants, which are also given in Appendix A.

The RKR method is a widely used first-order semiclassical inversion procedure for reconstructing the potential curve of a diatomic molecule electronic state, and the related theory is elaborated in a number of literatures and monographs [19–21,29,30]. A full derivation of the basic equations can be found in the reference [29]. The RKR method allows a step by step reconstruction of the potential curve until the corresponding experimental vibrational limit of the spectroscopic constants. Above the vibrational limit of the spectroscopic measurement, this method is no longer valid because the fitting of Dunham expansion becomes meaningless. While it is necessary to extrapolate this potential curve up to the dissociation limit in order to ensure the convergence of solving the radial Schrödinger equation. One popular method is called direct-potential-fit (DPF) analysis, which fits the RKR potential curve by a chosen theoretical potential (e.g. Morse or Lennard–Jones potential), insuring that such a potential curve exhibits a long-rang behavior as it approaches the dissociation limit. As proposed by Chauveau et al. [40] and da Silva et al. [18], the RKR potential curve is extrapolated by using a repulsive function $U_{rep}(r)$ for the shorter internuclear distance and a Hulburt and Hirschfelder potential $U_{HH}(r)$ [36] for the longer internuclear distance, which can accurately give continuous single-well potential curve. These two functions are written as [36]

$$U_{rep}(r) = \frac{a_1}{r^{b_1}} \tag{6}$$

$$U_{HH}(r) = D_e\left[1 - e^{-a_2(r-r_e)}\right]^2 + D_e[b_2 a_2^3 (r-r_e)^3 e^{-2a_2(r-r_e)} \times (1 + a_2 c_2 (r-r_e))] \tag{7}$$

where D_e and r_e refer to the dissociation energy of the electronic (relative to bottom of the potential energy curve) and the equilibrium internuclear distance, respectively, a_1, b_1, a_2, b_2 and c_2 are floating parameters that need to be adjusted to ensure continuity with the potential energy curve and they are adjusted in order that each extrapolation function fits a significant part of the extremity of the reconstructed potential energy curve, too.

In the RKR method, the key conclusions of this theory are made up of two Klein integrals (see Eqs (4) and (5) in Ref. [30]). The vibrational quantum numbers are treated as a continuous variable, in fact, the values of the vibrational quantum numbers are integers. Therefore, a much larger number of points are obtained than those obtained using integer values for a precise determination of the potential curve, resulting in the divergence of the Klein integrals at the neighborhood of the upper limit. To solve this problem, a Gauss-type quadrature method is used to obtain the potential curve near the upper limit [18]. Then, the potential curve is reconstructed with an iteration step of $\Delta v = 0.01$ until $v = 1$, and then with $\Delta v = 0.05$ until the experimental limit $v_{\max}$ (given in Appendix A). And the Klein integrals are integrated using a 128-point Gauss-type quadrature.

Once the overall potential curve has been obtained, the rovibrational level energies can be determined by solving the rotational dependence of the radial Schrödinger equation for a given electronic state n, which is given by [37]

$$\frac{d\psi_{v,J}(r)}{dr^2} + \frac{2\mu}{\hbar^2}\left[E_{n,v,J} - V_J(r)\right]\psi_{v,J}(r) = 0 \tag{8}$$

where $E_{n,v,J}$ is the rovibrational energy eigenvalue corresponding to the nuclear rovibrational wavefunction $\psi_{v,J}(r)$, and $V_J(r)$ is the effective potential curve, which is the sum of the rotationless potential and the centrifugal potential (see Eq. (12)). The Fourier

Grid Hamiltonian method proposed by Balint-Kurti and Marston [38,39] is used to resolve the level energies. The procedure uses an even number of grid points. And the Hamiltonian matrix elements are calculated using analytic formula described in Ref. [38], with the typographical correction indicated by da Silva [58].

It should be noted that the experimental values for higher levels are not available at the moment. Hence, the higher levels that corresponds to the long range potential are not supported by the experimental results. However, we can indirectly demonstrate the accuracy of the method by the published theoretical results in the literature. Le Roy et al. [25] pointed out that the Dunham-type parameters do not yield realistic predictions outside the valid range of the data used in the analysis, while the potential function obtained from the DPF treatment yields quantum mechanical accuracy over the data region and realistic predictions of the energies and properties of unobserved higher vibrational levels. And the long range potential of this work is considered to be accurate. Subsequently, da Silva et al. [18] calculated the potential curve of the N_2 ground state with the extrapolated Hulburt and Hirschfelder potential, which is in good agreement with that calculated by Le Roy *et al.* Hence, the extrapolated potential by Hulburt and Hirschfelder function is accurate based on the existing theories. The vibrational level energies by solving the radial Schrödinger equation over the RKR potential curve of N_2 ground electronic state were also presented by da Silva et al. [18], who compared the vibrational level energies with those obtained by Dunham expansion (shown in Fig. 2 of Ref. [18]) and concluded that the energies of the higher-lying levels are more accurate than the ones obtained by Dunham expansion. And the asymptotic behavior of the extrapolated potential is also validated by the dissociation limit in Fig. 2 of Ref. [18]. The same results are concluded by comparing the higher-lying levels obtained from extrapolated potential with those obtained from Dunham expansion in this paper.

2.3. Approach for the calculation of the maximum vibrational and rotational quantum numbers

The considered electronic states include all observed states up to their dissociation limits, and we have also taken into account the non-observed but theoretically predicted states. The summation of Eq. (5) must include all the vibrational states up to the dissociation limit and all the rotational levels below the energy of the dissociation limit of the rotating molecule. In Section 2.2, solving the rotational dependence of the radial Schrödinger equation, we obtain the rovibrational level energies $E_{n,v,J}$, which can be split into three contributions: the electronic excitation energy $E_{el}(n)$, the vibrational energy $E_{vib}(n,v)$ and the rotational energy $E_{rot}(n,v,J)$, given by

$$E_{n,v,J} = E_{el}(n) + E_{vib}(n, v) + E_{rot}(n, v, J) \tag{9}$$

For a given electronic state n, the maximum vibrational quantum number is determined by the following cut-off criterion [2]:

$$E_{vib}(n, v) < D_e(n) \tag{10}$$

where $D_e(n)$ refers to the rotationless dissociation energy of electronic state n relative to the minimum value of its potential curve. And the value of dissociation energy (given in Appendix A) is selected from the literature. It should be noted that for a few electronic states, the value of $E_{vib}(n,v)$ never exceeds the corresponding dissociation energy as the vibrational quantum number v becomes large. In this case, v_{max} is determined as the last vibrational quantum number before the derivative $\partial E_{vib}(n,v)/\partial v$ changes its sign, just as Babou et al. [2] did.

In analogy with what was done for the vibrational quantum number, the maximum allowed value J_{max} of the rotational quantum number for each vibrational quantum number $v \le v_{max}$ is determined by [2]:

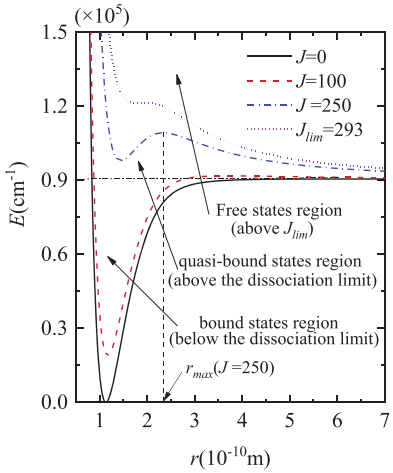

Fig. 2. Potential curve of the CO ground state $X^1\Sigma^+$ for different centrifugal distortions.

$$E_{vib}(n, v) + E_{rot}(n, v, J) \le V_J(r_{\max}(J)) \tag{11}$$

where $V_J(r)$ refers to the effective potential energy of the rotating molecule, and $r_{max}(J)$ is the local maximum position of the potential curve $V_J(r)$. Note that the rotation of diatomic molecule can also influence the dissociation energy. Specifically, the shape of potential curve is affected as the rotational quantum number increases, resulting in the increment of the D_e value. Hence, the right side of Eq. (11) is not D_e but $V_J(r_{max}(J))$. Under this circumstance, the bound and quasi-bound states are taken into account here. Fig. 2 shows the regions of the bound, quasi-bound and free states for the ground electronic state of CO.

Based on the classical mechanics, we must introduce an additional term in the expression of the RKR potential curve (or ab-initio potential curve in the literature) $U(r)$ to account for the effect of centrifugal force. Thus, the effective potential curve becomes:

$$V_J(r) = U(r) + \frac{\hbar^2 J(J+1)}{2\mu r^2} \tag{12}$$

where r is the internuclear distance of the diatomic molecule. After adding the rotational contribution to the overall reconstructed potential curve, we obtain a series of discrete potential energies versus the discrete internuclear distances for a specific J value. Then the cubic spline is used to interpolate the discrete potential energies over the discrete internuclear distances. Thus, a series of potential curves can be reconstructed for different rotational quantum numbers. For J=0, the rotationless potential is obtained. As the quantum number increases, the position of the minimum for the potential curve moves up and the dimension of the potential well decreases. When J reaches the value $J_{\lim}$, the potential curve does not exhibit a local minimum and is entirely repulsive. And there are no stable states with J larger than J_{lim}. Hence, the centrifugal distortion of the potential determines the existence of the quasi-bound states above the dissociation limit of the molecule due to rotation. In order to obtain the J_{max} value for each vibrational quantum number, the J_{lim} value must be determined, which is characterized by a negative derivative with respect to the internuclear distance. So the rotational quantum number is changed successively until the condition below is reached:

$$\frac{\partial V_J(r)}{\partial r} < 0. \tag{13}$$

Mathematically, for each $J<J_{lim}$, $r_{max}(J)$ is determined by [2]

$$\left.\frac{\partial V_J(r)}{\partial r}\right|_{r=r_{\max}(J)} = 0, \tag{14}$$

$$\left.\frac{\partial^2 V_J(r)}{\partial r^2}\right|_{r=r_{\max}(J)} < 0. \tag{15}$$

In the practical calculation, for each J, we start with a large r value (for example, $r=0.6$ nm), then we decrease the r value (r-Δr) until the condition $V(r)$-$V(r$-$\Delta r)>0$ (Δr is the decrement) is reached. The obtained $r_{max}(J)$ value is introduced into Eq. (11) to determine a J_{max} for each v. However, as Babou et al. [2] mentioned, for some states, a constraint must be imposed to obtain the J_{max} value, given by

$$J_{\max}(v+1) \le J_{\max}(v) \tag{16}$$

It should be noted that quasi-bound states are not really bound and their energies cannot be calculated simply by solving the Schrödinger equation in principle, but the lifetime of the quasi-bound states is very difficult to be determined by calculating resonances. Hence, the J_{max} is determined analytically in this paper. Once the maximum vibrational quantum number for each electronic state and the maximum rotational quantum number for each vibrational state have been determined, the internal partition function can be calculated using Eq. (5).

3. Equilibrium thermodynamic properties

3.1. Theoretical aspects

Once the internal partition function Q_{int} has been obtained, it is easy to calculate all the internal thermodynamic properties of the components according to the formulae of statistical thermodynamics [23]. For 1 mol of an ideal gas at the equilibrium temperature T, the average internal energy E_{int} is obtained from the first derivative of Q_{int}

$$E_{\text{int}}(T) = RT^2\left(\frac{\partial lnQ_{\text{int}}(T)}{\partial T}\right) \tag{17}$$

and the internal specific heat is calculated from the second derivative of Q_{int}

$$C_{p,\text{int}}(T) = \frac{\partial E_{\text{int}}(T)}{\partial T} = R\left[2T\left(\frac{\partial lnQ_{\text{int}}}{\partial T}\right) + T^2\left(\frac{\partial^2 lnQ_{\text{int}}}{\partial T^2}\right)\right] \tag{18}$$

where R is the gas constant (R=0.69502 cm^{-1} K^{-1} when the E_i is given by the spectroscopic level in unit of cm^{-1}, $R=k_B/hc$). E_{int} and $C_{p,int}$ are expressed as dimensionless quantities $\bar{E}_{\text{int}}(T) = E_{\text{int}}(T)/RT$ and $\bar{C}_{p,\text{int}}(T) = C_{p,\text{int}}(T)/R$, respectively.

Expanding the Eqs (17) and (18), the average internal energy and the internal specific heat are expressed as

$$E_{\text{int}}(T) = Q_{\text{int}}(T)^{-1} \times \sigma \sum_{n}^{n_{\max}} (2-\delta_{\Lambda,0})(2S+1) \sum_{v}^{v_{\max}} \sum_{J}^{J_{\max}} (2J+1) \times \left(E_{n,vJ}-\varepsilon_0\right) \exp\left(-\frac{E_{n,vJ}-\varepsilon_0}{RT}\right) \tag{19}$$

$$C_{p,\text{int}}(T) = \frac{1}{RT^2}\left\{\left\langle \left(E_{n,vJ}-\varepsilon_0\right)^2\right\rangle - E_{\text{int}}^2(T)\right\} \tag{20}$$

where,

$$\left\langle \left(E_{n,vJ}-\varepsilon_0\right)^2\right\rangle = Q_{\text{int}}(T)^{-1} \times \sigma \sum_{n}^{n_{\max}} (2-\delta_{\Lambda,0})(2S+1) \sum_{v}^{v_{\max}} \sum_{J}^{J_{\max}} (2J+1) \times \left(E_{n,vJ}-\varepsilon_0\right)^2 \exp\left(-\frac{E_{n,vJ}-\varepsilon_0}{RT}\right) \tag{21}$$

3.2. Results and discussions

To obtain the thermodynamic properties, it is very important to select the spectroscopic constants, which are compared with those adopted by McBride et al. [16], Capitelli et al. [7] and Babou et al. [2]. According to the work of Babou et al. [2], two points are concluded. one is that the spectroscopic constants selected include more anharmonic correction terms and rotational constants, the other is that the same rovibrational structures for high-lying electronic states as for the ground state or for the last known electronic state doesn't need to be assumed due to the recent publications of the spectroscopic constants of these electronic states. Note that the ab-initio potential curves for some higher-lying electronic states are obtained from the literature.

The cut-off criterion, the rovibrational interaction and excited electronic states play important roles in determining the partition functions and thermodynamic properties. The cut-off criterion is related to the dissociation energy of each electronic state for a diatomic molecule. Through the solution of the rotational dependence of the radial Schrödinger equation, the rovibrational interaction is considered and the rovibrational energies for higher-lying levels are more accurate than those obtained by the Dunham expansion. All available excited electronic states (especially higher-lying electronic states that can be found in the literature) are considered in this paper. Table 1 compares the three quantities adopted in this paper with those from Refs. [2,7,16] for N_2^+. Theoretically, the results we obtain are more accurate, since the electronic states we selected are more detailed and the calculated level energies are more accurate for higher-lying levels at high temperatures.

Fig. 3 compares the internal partition functions and the internal specific heats in this work with those from Refs. [2,7,16] for N_2, N_2^+, NO, O_2, CN, C_2, CO and CO^+ diatomic molecules in the temperatures from 100 to 50000 K. The internal partition functions increase with the increasement of the temperature. The internal specific heats start from the value 1, which is due to the activation of the rotational degrees of freedom, and then the internal specific heats rapidly reach value 2, which includes the vibrational contribution from the ground electronic state. In order to analyze the effect of different number of electronic states on the internal specific heat, we calculate the contributions of the electronic ground state and the excited states to the internal specific heat of CN (shown in Fig. 4). The curve (a) in Fig. 4 denotes the internal specific heat of the ground state, which increases rapidly from the value 1 to the value 2 due to the same reasons mentioned above. The successive internal specific heats considering different numbers of electronic excited states are shown in curves (b)-(d), which show the important role of electronic excited states.

As shown in Fig. 3, the partition functions of N_2, N_2^+, NO, O_2, CN, C_2, CO and CO^+ agrees well with those from Ref. [16] which only gives the partition functions up to 20000 K. Moreover, our calculated partition functions of N_2, NO and O_2 are in excellent agreement with those from Refs. [2,7] up to 50000 K. These calculations are all based on the same number of electronic states, and the slight differences of about 5% between our results and those of Refs. [2,7] may come from the different treatment methods in calculating the level energies. For CN molecule, our calculated results are in excellent agreement with those of Ref. [2], and slight differences occur at high temperatures due to the same reason as N_2, NO and O_2. Our results are slightly higher than the values from Ref. [7] at high temperatures because we have considered more high-lying electronic levels that are more accurate. Similarly, the results of C_2 we obtained are slightly higher than the ones of Refs. [2,7]. For CO molecule, our results are higher than the values from Ref. [7], but lower than the values from Ref. [2] since we have considered different high-lying electronic levels. Note that the higher

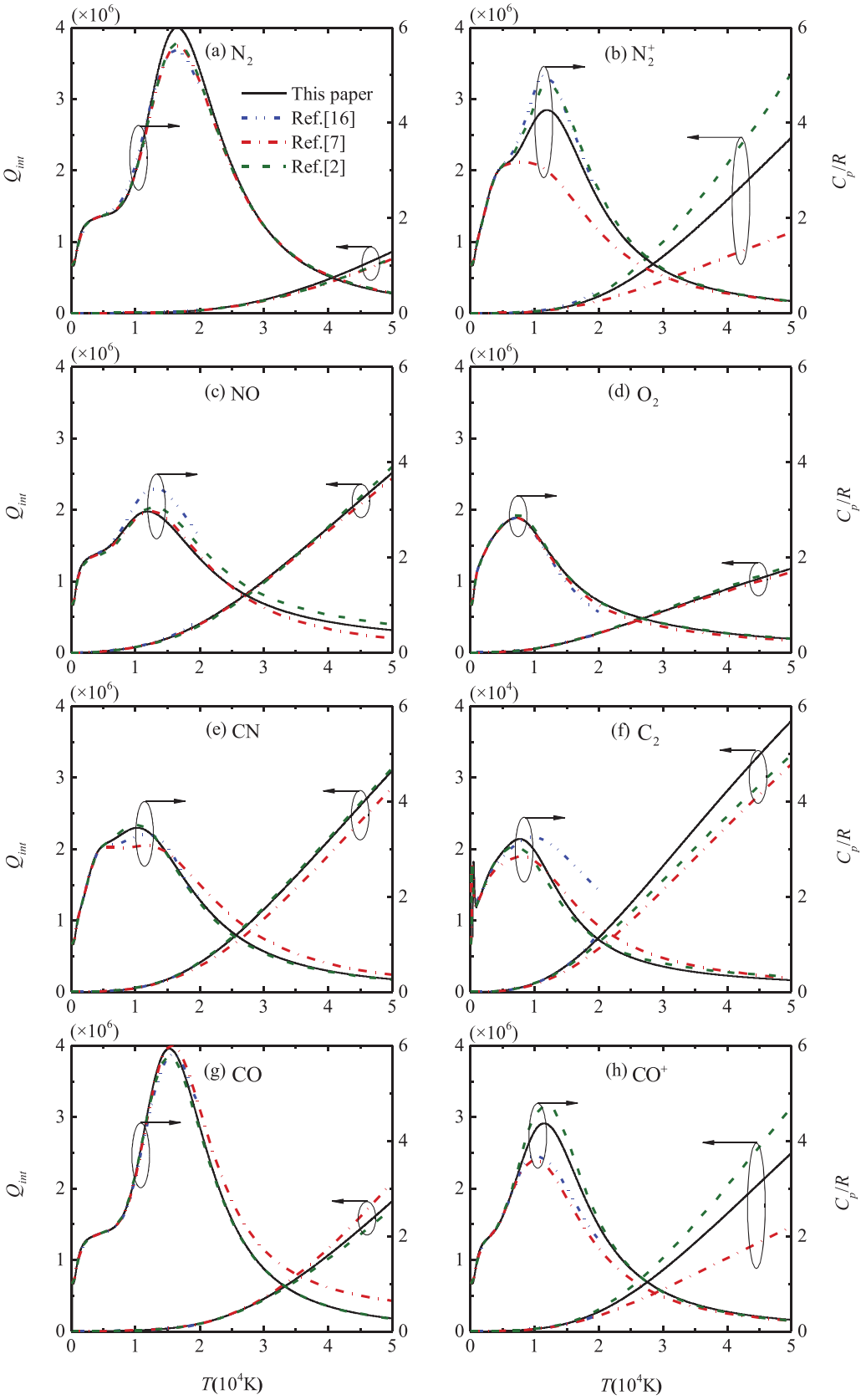

Fig. 3. Comparison of the internal partition functions and the internal specific heats in this work with those from Refs. [2,7,16] for **(a)** N_2, **(b)** N_2^+, **(c)** NO, **(d)** O_2, **(e)** CN, **(f)** C_2, **(g)** CO, **(h)** CO^+. Note that the data from Ref. [16] are only fitted to 20000 K.

Table 1
Comparison of the number of the electronic states, cut-off criterion and method for calculating energies adopted in this paper with those from Refs. [2,7,16] for N_2^+.

	This paper	Ref. [16]	Ref. [7]	Ref. [2]
The number of electronic states	16	6	7	16
The cut-off criterion	Eqs. (10) and (11)	×	Eqs. (10) and (11)	Eqs. (10) and (11)
Method for calculating energies	Improved method	Dunham expansion	Dunham expansion	Dunham expansion
Maximum partition function	4.27	5	3.17	4.75

Table 2
Percentage contributions to $Q_{int}(T)$ of the last (n_{max}-th) electronic state (PC1, for short), the last two electronic states (PC2, for short) and the last three electronic states (PC3, for short) at 10000 K, 20000 K, 30000 K, 40000 K and 50000 K.

	Molecule	N_2	O_2	N_2^+	NO	CN	C_2	CO	CO^+
	n_{max}	11	21	16	16	16	20	11	8
PC1(%)	T = 10000K	0.001	0.011	0.004	0.000	0.006	0.000	0.000	0.017
	T = 20000K	0.178	0.388	0.198	0.065	0.273	0.039	0.006	0.259
	T = 30000K	0.422	0.810	0.500	0.275	0.691	0.171	0.012	0.414
	T = 40000K	0.543	1.076	0.730	0.537	1.019	0.348	0.015	0.483
	T = 50000K	0.605	1.245	0.886	0.786	1.258	0.526	0.017	0.518
PC2(%)	T = 10000K	0.012	0.018	0.045	0.001	0.031	0.002	0.001	0.072
	T = 20000K	1.768	0.677	2.042	0.114	0.986	0.207	0.062	0.992
	T = 30000K	4.066	1.493	5.222	0.494	2.199	0.881	0.129	1.533
	T = 40000K	5.148	2.052	7.647	0.980	3.045	1.770	0.163	1.760
	T = 50000K	5.681	2.433	9.308	1.450	3.621	2.663	0.182	1.871
PC3(%)	T = 10000K	0.020	0.050	0.052	0.001	0.045	0.003	0.054	0.803
	T = 20000K	2.105	1.497	2.248	0.146	1.313	0.340	2.413	9.597
	T = 30000K	4.575	3.050	5.663	0.627	2.849	1.422	4.265	14.146
	T = 40000K	5.668	4.028	8.236	1.239	3.894	2.840	5.009	15.868
	T = 50000K	6.186	4.662	9.986	1.830	4.593	4.256	5.372	16.634

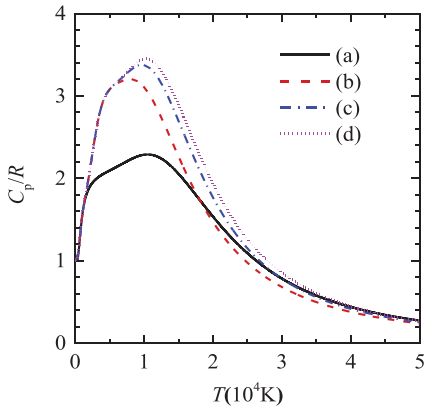

Fig. 4. Contributions of **(a)** the ground state, **(b)** the ground state and the successive 4 excited states, **(c)** the ground state and the successive 9 excited states, **(d)** the ground state and the successive 16 excited states, to the dimensionless specific heat as a function of temperature for CN.

excited electronic states of CO are not taken into account in this paper because of the absence of accurate spectroscopic constants or potential curves. The differences between our partition functions and those from Refs. [2,7] are much larger for the remaining two molecules. For N_2^+, Our partition functions obtained by considering 16 electronic states are larger than the values of Ref. [7] that are obtained using only 7 electronic states. However, our results are also lower than the values of Ref. [2], although they are based on the same electronic states. This difference between our results and those of Ref. [2] is probably due to the different methods for calculating the energies of rovibrational levels, especially those of higher-lying levels. For CO^+, our predictions are higher than the values from Ref. [7] and lower than the values from Ref. [2] although they are obtained from the same electronic states. We found no satisfactory explanation for this behavior except the different calculations of level energies.

The differences between the present specific heats and the results from Refs. [2,7,16] are also shown in Fig. 3. Larger differences can be observed near the peaks. It means that the number of electronic excited states considered has a larger impact on the maximum internal specific heats. Beyond this temperature range, our calculated internal partition functions are in good agreement with those from Refs. [2,7,16] except for NO, CN and CO molecules. However, our results are within the values from Refs. [2,7] at high temperatures for these three molecules.

Overall, different sources of thermodynamic properties for diatomic molecules at high temperatures exhibit significant discrepancies depending on the cut-off criterion, rovibrational interaction energy and the number of electronic states. The electronic excitation is more effective than high vibrational excitation of the electronic state. But the effect of the high vibrational excitation on the partition function is non-negligible at high temperatures, especially for N_2^+, C_2, CO^+. Theoretically, the results we obtained are more accurate since we have selected the more detailed and accurate electronic states, and our calculated level energies are more accurate for high-lying levels at high temperatures. A full understanding of the three factors will obtain more accurate thermodynamic properties.

4. Non-equilibrium thermodynamic properties

The high-temperature flow field related to hypersonic flights is usually in thermal and chemical non-equilibrium. When dealing with practical non-equilibrium entry flows, two-temperature model (one of the multi-temperature model) is the primary choice due to its easier treatment in mathematics. Based on the two-temperature model and the rovibrational energy partitioning scheme proposed by Jaffe [5], two-temperature thermodynamic properties of diatomic molecules are studied and analyzed in this section, which can be extended to the multi-temperature model, the state-to-state model or even more accurate models.

4.1. Theoretical aspects

The general form of the diatomic level energy is given by Eq. (9), which can be expanded as:

$$E_{n,v,J}=E_{el}(n)+E_{vib}(n,v)+E_{rot}(n,J)+E_{inter}(n,v,J) \tag{22}$$

Based on the two-temperature model, Jaffe [5] proposed two ways of splitting the rovibrational internal energy corresponding to two limiting cases, i.e., the interaction energy $E_{inter}(n,v,J)$ is assigned fully either to the vibrational energy or to the rotational energy, which are expressed as follows [5]:

$$\Delta^{I}E(v,J)=E_{rot}(n,J)+E_{inter}(n,v,J) \tag{23}$$

$$\Delta^{II}E(v,J)=E_{vib}(n,v)+E_{inter}(n,v,J) \tag{24}$$

where $E_{vib}(n,v)$ is the vibrational energy depending only on v, and $E_{rot}(n,J)$ is the part of $E_{rot}(n,v,J)$ depending exclusively on J. The corresponding two-temperature partition functions are given by [5]

$$Q_{int}^{I}(T_v,T_r)=\sigma\sum_{n=0}^{n_{\max}}(2-\delta_{\Lambda,0})(2S+1)e^{-\frac{E_{el}(n)}{RT_v}}\times\left[\sum_{v=0}^{v_{\max}(n)}e^{-\frac{E_{vib}(n,v)-\varepsilon_0}{RT_v}}\times\left(\sum_{J=0}^{J_{\max}(n,v)}(2J+1)e^{-\frac{\Delta^{I}E(v,J)}{RT_r}}\right)\right] \tag{25}$$

$$Q_{int}^{II}(T_v,T_r)=\sigma\sum_{n=0}^{n_{\max}}(2-\delta_{\Lambda,0})(2S+1)e^{-\frac{E_{el}(n)}{RT_v}}\times\left[\sum_{J=0}^{J_{\max}(n)}(2J+1)e^{-\frac{E_{rot}(n,J)}{RT_r}}\times\left(\sum_{v=0}^{v_{\max}(n,J)}e^{-\frac{\Delta^{II}E(v,J)-\varepsilon_0}{RT_v}}\right)\right] \tag{26}$$

respectively. The two-temperature internal energy $E_{int}(T_v,T_r)$ can be given by

$$E_{\text{int}}(T_v,T_r)=R\left[T_v^2\frac{\partial \ln Q_{\text{int}}(T_v,T_r)}{\partial T_v}+T_r^2\frac{\partial \ln Q_{\text{int}}(T_v,T_r)}{\partial T_r}\right] \tag{27}$$

and the specific heats of vibration and rotation are respectively defined by

$$C_{p,vib}(T_v,T_r)=\frac{\partial E_{\text{int}}(T_v,T_r)}{\partial T_v} \tag{28}$$

$$C_{p,rot}(T_v,T_r)=\frac{\partial E_{\text{int}}(T_v,T_r)}{\partial T_r} \tag{29}$$

the vibrational and rotational specific heats depend on both T_v and T_r. Here, we introduce the dimensional internal energy, which is defined by

$$\tilde{E}_{\text{int}}=\frac{E_{\text{int}}(T_v,T_r)}{\sqrt{T_vT_r}} \tag{30}$$

For the first limiting case, the two-temperature internal energy (Eq. (27)) can be expanded as

$$E_{int}^{I}(T_v,T_r)=\frac{1}{Q_{int}^{I}(T_v,T_r)}\times\sigma\sum_{n=0}^{n_{\max}}(2-\delta_{\Lambda,0})(2S+1)e^{-\frac{E_{el}(n)}{RT_v}}\times\left[\sum_{v=0}^{v_{\max}(n)}e^{-\frac{E_{vib}(n,v)-\varepsilon_0}{RT_v}}\times\left(\sum_{J=0}^{J_{\max}(n,v)}(2J+1)\times E_{n,v,J}\times e^{-\frac{\Delta^{I}E(v,J)}{RT_r}}\right)\right] \tag{31}$$

and the vibrational and rotational specific heats can be respectively extended as

$$C_{p,vib}^{I}(T_v,T_r)=\frac{1}{RT_v^2}\left\{\left\langle E_{n,v,J}\times(E_{el}(n)+E_{vib}(n,v)-\varepsilon_0)\right\rangle-\left\langle E_{el}(n)+E_{vib}(n,v)-\varepsilon_0\right\rangle\times E_{int}^{I}(T_v,T_r)\right\} \tag{32}$$

$$C_{p,rot}^{I}(T_v,T_r)=\frac{1}{RT_r^2}\left\{\left\langle E_{n,v,J}\times\Delta^{I}E(v,J)\right\rangle-\left\langle\Delta^{I}E(v,J)\right\rangle\times E_{int}^{I}(T_v,T_r)\right\} \tag{33}$$

where,

$$\langle\Re\rangle=\frac{1}{Q_{int}^{I}(T_v,T_r)}\times\sigma\sum_{n=0}^{n_{\max}}(2-\delta_{\Lambda,0})(2S+1)e^{-\frac{E_{el}(n)}{RT_v}}\times\left[\sum_{v=0}^{v_{\max}(n)}e^{-\frac{E_{vib}(n,v)-\varepsilon_0}{RT_v}}\times\left(\sum_{J=0}^{J_{\max}(n,v)}(2J+1)\times\Re\times e^{-\frac{\Delta^{I}E(v,J)}{RT_r}}\right)\right] \tag{34}$$

where, $\Re$ refers to the energy in $\langle\rangle$. The formulas of the internal energy and the internal specific heats for the second limiting case can also be obtained by similar derivation.

4.2. Results and discussions

The accuracy of the rovibrational level energies has been demonstrated by the results at equilibrium. In order to verify the accuracy of computational procedure for calculating the non-equilibrium thermodynamic properties, we calculate the vibrational specific heat of N_2 according to the first energy partitioning scheme given by Eq. (23) and compares with the results from Ref. [44]. Our calculated vibrational specific heats are slightly higher than the ones of Ref. [44], but shows similar distribution trend to Ref. [44], which validates our calculated thermodynamic properties.

Figs. 5–12 show the cloud maps of the two-temperature internal partition functions, the dimensionless internal energies, the dimensionless vibrational and rotational specific heats of N_2, N_2^+, NO, O_2, CN, C_2, CO and CO^+ diatomic molecules versus vibrational and rotational temperatures (T_v and T_r) for the two energy partitioning schemes defined by Eqs. (23) and (24), respectively. We limit our discussion to CN molecule, similar conclusions can be drawn for other diatomic molecules considered here. As shown in Fig. 9(a), the partition functions calculated according to the two energy partitioning schemes are very similar, the slight differences mainly come from the interaction energy E_{inter}, which is generally negative. With such a remarkable feature, E_{inter} can also explain the behavior observed on the maps of the dimensionless internal energies, i.e., the values calculated by Eq. (23) are larger (lower) than the ones calculated by Eq. (24) for T_r larger (lower) than T_v, which were also presented by Babou et al. [2] as shown in Fig. 9(b). Besides, the deviations between the values according to the two schemes for high T_v and low T_r are lower than the ones for high T_r and low T_v. This phenomenon was also explained by Babou et al. [2] due to the higher electronic and vibrational energy contributions than the rotational ones.

Overall, the internal partition function and the dimensionless internal energy are weakly affected by the energy partitioning schemes adopted. On the contrary, the specific heat is more sensitive to the two energy partitioning schemes due to the definition by derivative of the internal energy. For the vibrational specific heats shown in Fig. 9(c), the results obtained using these two schemes appear to be qualitatively similar. By a close inspection,

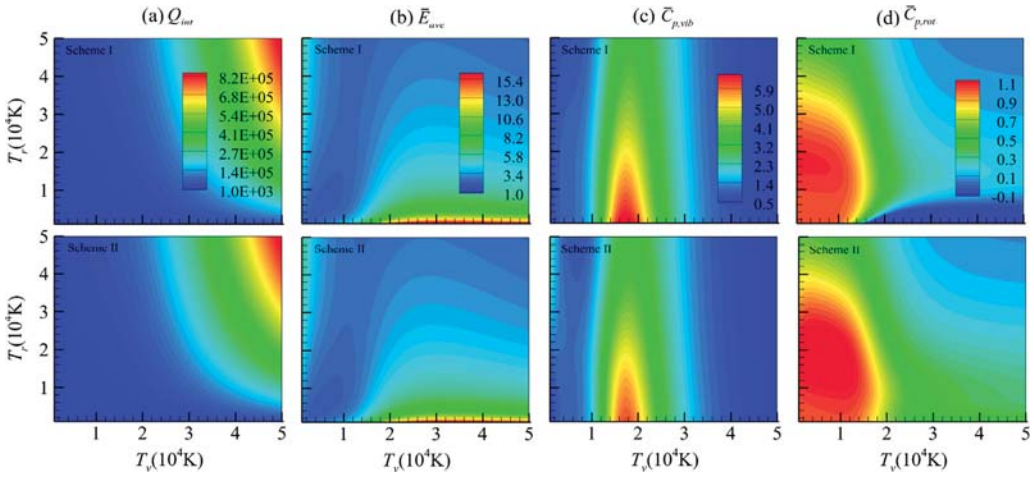

Fig. 5. Contours of **(a)** the internal partition functions, **(b)** the dimensionless internal energies, **(c)** the dimensionless vibrational specific heat and **(d)** the dimensionless rotational specific heat for N_2 versus vibrational (T_v) and rotational (T_r) temperatures according to the first energy partitioning scheme (scheme I) defined by Eq. (23) and the second energy partitioning scheme (scheme II) defined by Eq. (24).

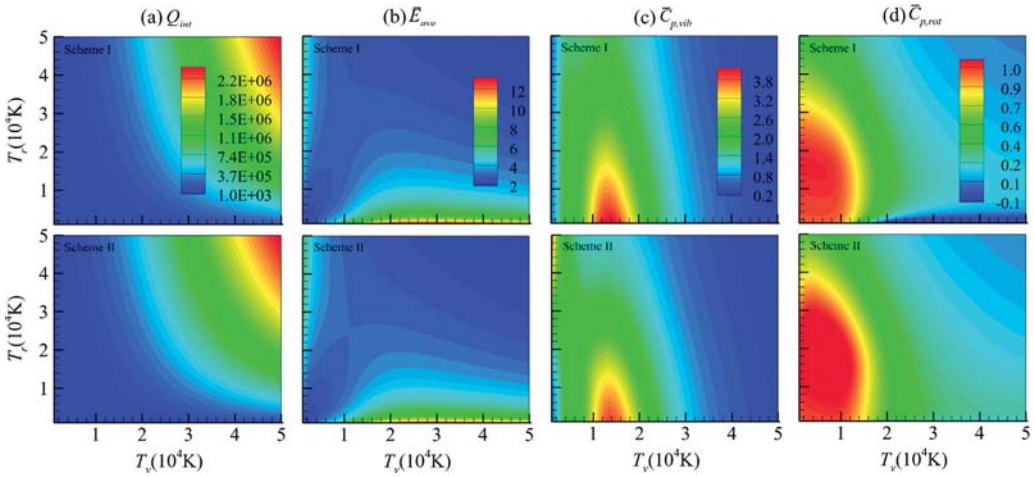

Fig. 6. Contours of **(a)** the internal partition functions, **(b)** the dimensionless internal energies, **(c)** the dimensionless vibrational specific heat and **(d)** the dimensionless rotational specific heat for N_2^+ versus vibrational (T_v) and rotational (T_r) temperatures according to the first energy partitioning scheme (scheme I) defined by Eq. (23) and the second energy partitioning scheme (scheme II) defined by Eq. (24).

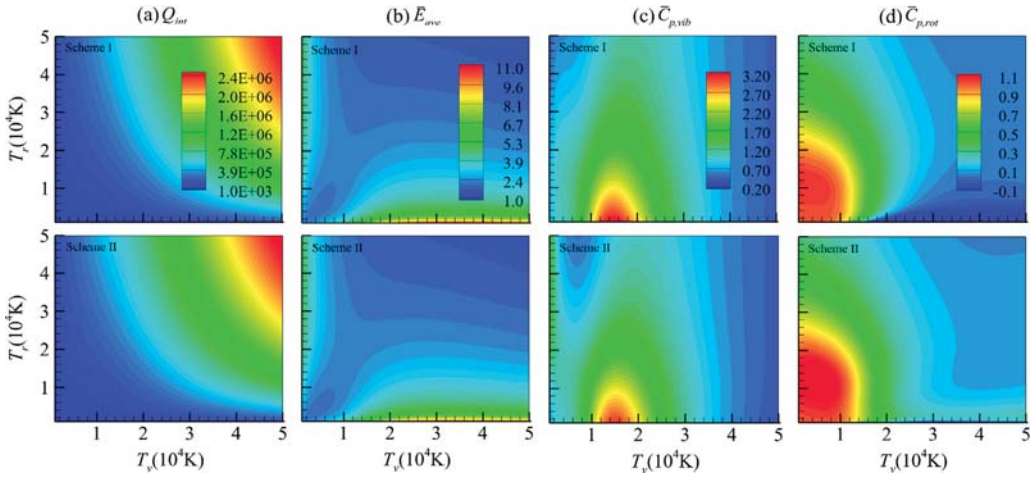

Fig. 7. Contours of **(a)** the internal partition functions, **(b)** the dimensionless internal energies, **(c)** the dimensionless vibrational specific heat and **(d)** the dimensionless rotational specific heat for NO versus vibrational (T_v) and rotational (T_r) temperatures according to the first energy partitioning scheme (scheme I) defined by Eq. (23) and the second energy partitioning scheme (scheme II) defined by Eq. (24).

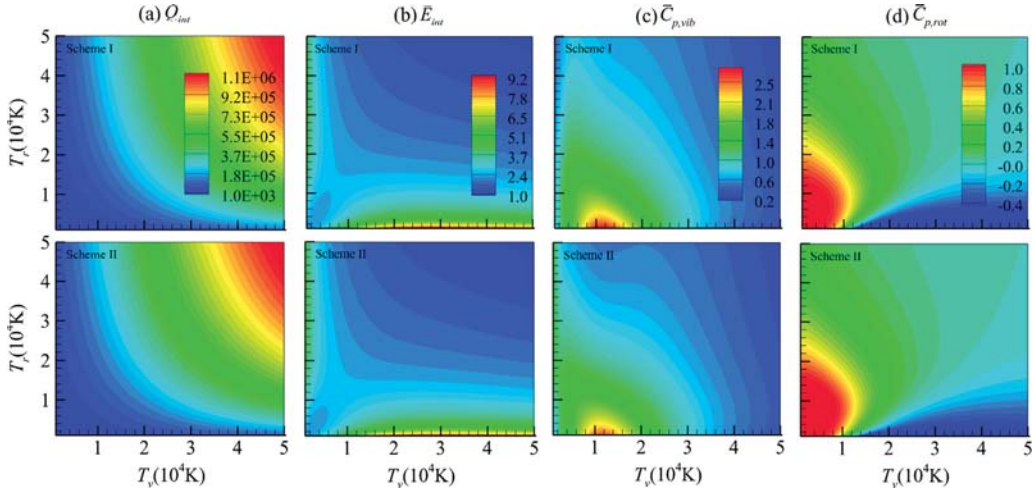

Fig. 8. Contours of **(a)** the internal partition functions, **(b)** the dimensionless internal energies, **(c)** the dimensionless vibrational specific heat and **(d)** the dimensionless rotational specific heat for O_2 versus vibrational (T_v) and rotational (T_r) temperatures according to the first energy partitioning scheme (scheme I) defined by Eq. (23) and the second energy partitioning scheme (scheme II) defined by Eq. (24).

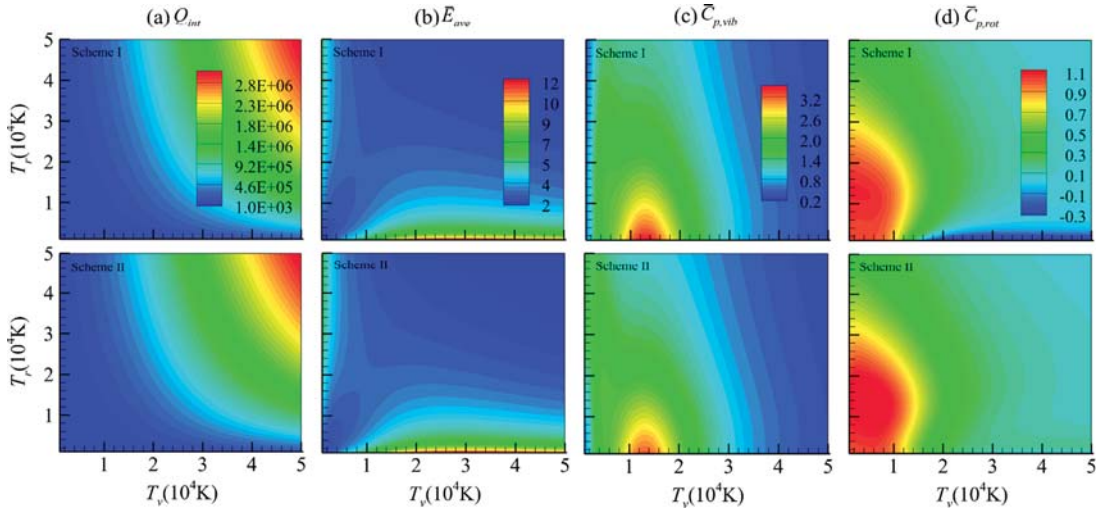

Fig. 9. Contours of **(a)** the internal partition functions, **(b)** the dimensionless internal energies, **(c)** the dimensionless vibrational specific heat and **(d)** the dimensionless rotational specific heat for CN versus vibrational (T_v) and rotational (T_r) temperatures according to the first energy partitioning scheme (scheme I) defined by Eq. (23) and the second energy partitioning scheme (scheme II) defined by Eq. (24).

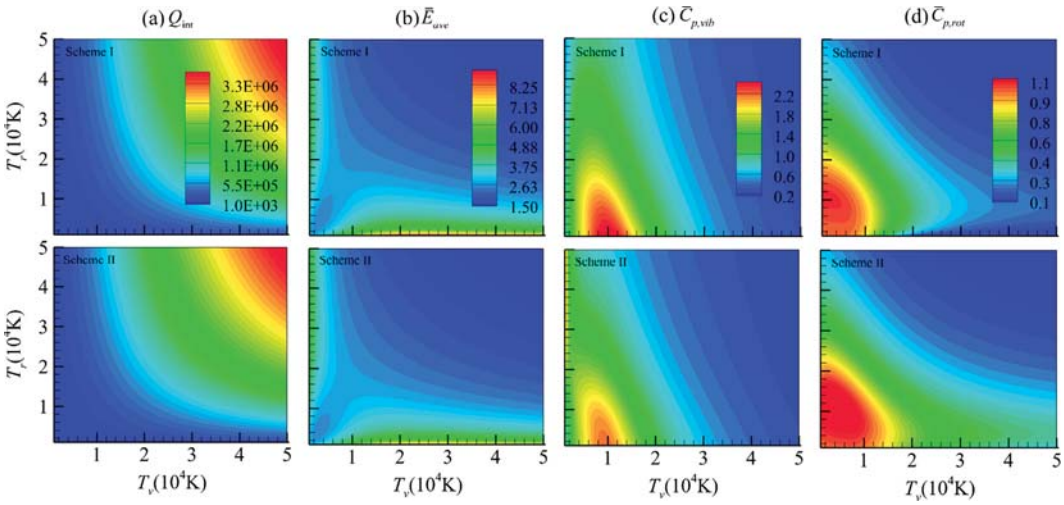

Fig. 10. Contours of **(a)** the internal partition functions, **(b)** the dimensionless internal energies, **(c)** the dimensionless vibrational specific heat and **(d)** the dimensionless rotational specific heat for C_2 versus vibrational (T_v) and rotational (T_r) temperatures according to the first energy partitioning scheme (scheme I) defined by Eq. (23) and the second energy partitioning scheme (scheme II) defined by Eq. (24).

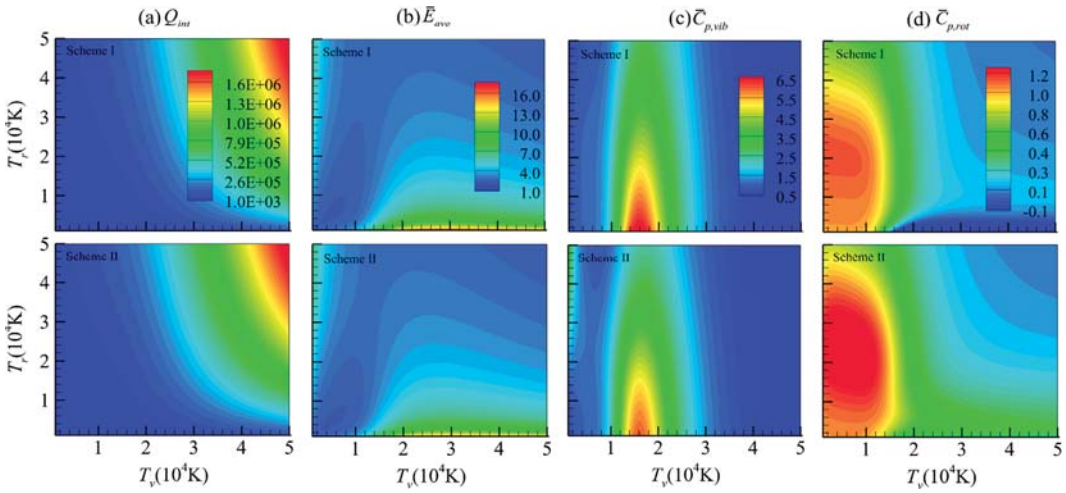

Fig. 11. Contours of **(a)** the internal partition functions, **(b)** the dimensionless internal energies, **(c)** the dimensionless vibrational specific heat and **(d)** the dimensionless rotational specific heat for CO versus vibrational (T_v) and rotational (T_r) temperatures according to the first energy partitioning scheme (scheme I) defined by Eq. (23) and the second energy partitioning scheme (scheme II) defined by Eq. (24).

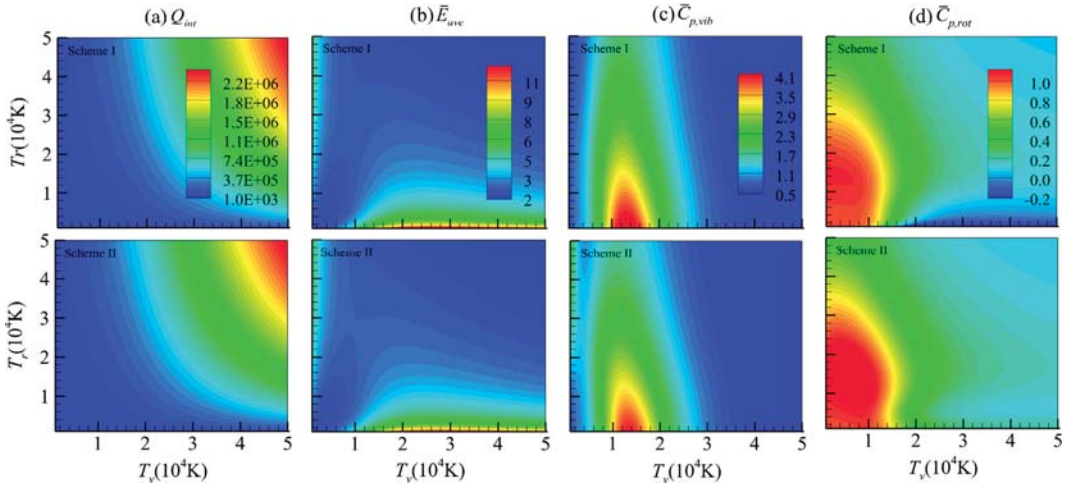

Fig. 12. Contours of **(a)** the internal partition functions, **(b)** the dimensionless internal energies, **(c)** the dimensionless vibrational specific heat and **(d)** the dimensionless rotational specific heat for CO^+ versus vibrational (T_v) and rotational (T_r) temperatures according to the first energy partitioning scheme (scheme I) defined by Eq. (23) and the second energy partitioning scheme (scheme II) defined by Eq. (24).

it can be found that the larger discrepancies occur in the part corresponding to high T_r and low T_v. For the rotational specific heat shown in Fig. 9(d), the major discrepancies occur in the part corresponding to high T_v and low T_r. The reasons for such discrepancies of the vibrational (rotational) specific heat can be found in the definition and in the relative importance between the vibrational (rotational) energy and the interaction energy. First, $C_{p,vib}$ ($C_{p,rot}$) strongly depends on T_v (T_r), while it weakly depends on T_r (T_v). Second, the relative importance between the vibrational (rotational) energy and the interaction energy changes with T_v and T_r. In the case of lower T_v (T_r) and higher T_r (T_v), the interaction energy becomes comparable with the vibrational (rotational) energy, leading to the different results for the two energy partitioning schemes. This phenomenon can be clearly seen by defining a variable δ, which is given by

$$\delta = \left| X^{\mathrm{I}} - X^{\mathrm{II}} \right| \tag{35}$$

where X denotes $C_{p,int}$ or $C_{p,rot}$, the superscripts I and II refer to the first and second energy partitioning scheme, respectively. An example for CN is shown in Fig. 13. It should be noted that the rotational specific heat calculated according to the first energy partitioning scheme is negative for high T_v and low T_r. This phenomenon was also observed by Jaffe [5] and explained by Babou et al. [2], who pointed that the vibrational energy contribution to the rotational specific heat is negative. Moreover, higher rotational levels usually correspond to lower vibrational levels due to dissociation, which leads to a decrease of the average vibrational energy as T_r increases.

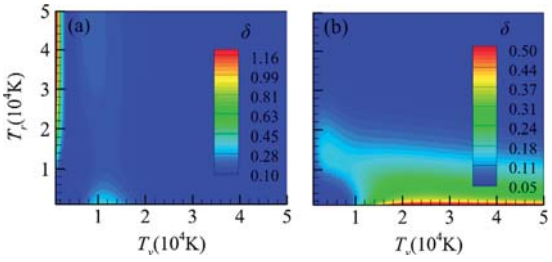

Fig. 13. The differences of (a) the two-temperature vibrational specific heat and (b) the two-temperature rotational specific heat between the two energy partitioning schemes for CN.

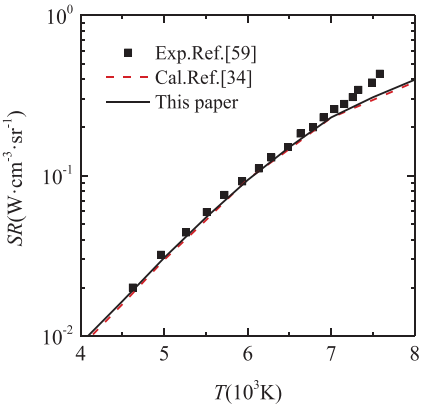

Fig. 14. Comparison of the total radiative source strength versus temperature between our results and the ones of Refs. [34,59] for air plasma at atmosphere pressure with the number densities of N_2, N_2^+, O_2, NO from Ref. [59].

5. Spectral radiative properties

The spectral radiative properties of the high-temperature gases are important in radiative transfer calculations for hypersonic flights. The emission coefficient ε_v and the absorption coefficient κ_v of diatomic discrete transition are given respectively [34,35]

$$\varepsilon_v = \sum_{ul} \frac{A_{ul}}{4\pi} hc\nu_{ul} N_u f_{ul}(\nu - \nu_{ul}) \tag{36}$$

$$\kappa_v = \sum_{ul} (N_l B_{lu} - N_u B_{ul}) h\nu_{ul} f_{ul}(\nu - \nu_{ul}) \tag{37}$$

where A_{ul}, B_{lu} and B_{ul} are the Einstein coefficient of the upper level u and lower level l, ν_{ul} is the wavenumber, $f_{ul}(\nu\text{-}\nu_{ul})$ is the spectral line shape of the transition, N_u and N_l denotes the population of the upper transition level and the lower transition level, respectively. In thermodynamic equilibrium, the population of the level can be described by a Boltzmann distribution, given by

$$N_u = N_{total} g \frac{2J+1}{Q_{int}(T)} exp\left(-\frac{E_{n,v,J}}{kT}\right) \tag{38}$$

where N_{total} is the total population of the considered molecule, g is the nuclear spin factor, and $Q_{int}(T)$ is the internal partition function. In thermodynamic non-equilibrium, when adopting three-temperature model (the electronic temperature T_e is introduced into the two-temperature model to represent the temperature of the electronic energy levels with a Boltzmann distribution), N_u is

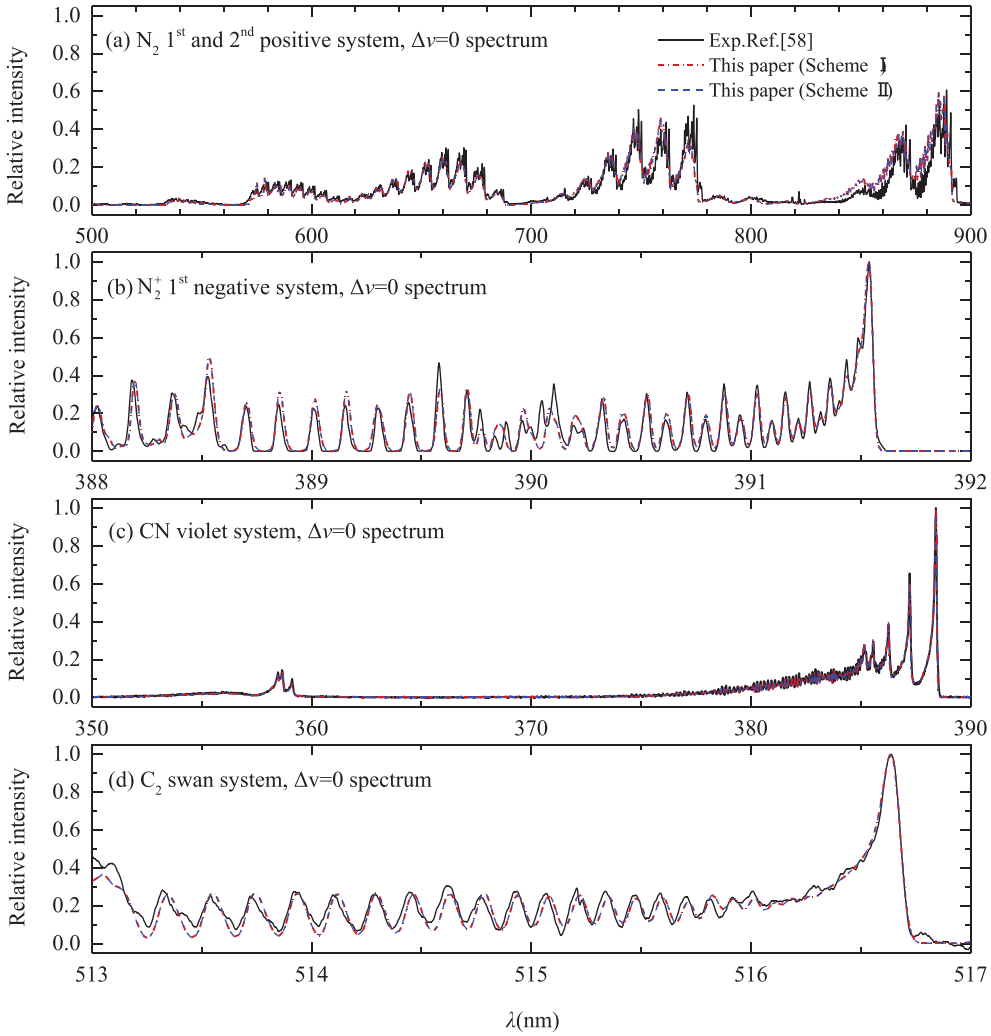

Fig. 15. Comparison of the relative spectral radiative intensity with the experimental data from Ref. [58] **(a)** for N_2 first and second positive Δv=0 systems at T_e=1000 K, T_v=8500 K and T_r=1500 K, **(b)** for N_2^+ first negative Δv=0 system at T_e=2000 K, T_v=8000 K and T_r=4500 K, **(c)** for CN violet Δv=0 system at $T_e = T_v = T_r$ = 6050 K and **(d)** for C_2 swan Δv=0 system at $T_e = T_v$ = 8000 K and T_r = 6500 K.

Table 3
Radiative source strength per molecule (W•sr^{-1}•molecule^{-1}) for CN: comparison with the calculated results.

T(K)	Electronic system	This paper	Results from [41]	Results from [43]
1000	Red	5.109E – 21	5.442E – 21	5.361E – 21
	Violet	4.583E – 29	4.858E – 29	4.798E – 29
	LeBlanc	1.359E – 31	1.398E – 31	1.367E – 31
5000	Red	2.096E – 16	2.376E – 16	2.297E – 16
	Violet	2.957E – 16	3.193E – 16	3.130E – 16
	LeBlanc	1.460E – 18	1.495E – 18	1.469E – 18
10000	Red	5.577E – 16	7.669E – 16	6.285E – 15
	Violet	7.951E – 15	8.414E – 15	8.203E – 15
	LeBlanc	6.782E – 17	7.217E – 17	6.837E – 17

Table 4
Radiative source strength per molecule (W•sr^{-1}•molecule^{-1}) for C_2: comparison with the calculated results.

T(K)	Electronic system	This paper	Results from [33]	Results from [41]	Results from [43]
1000	Philips	3.765E – 21	3.94E – 21	3.821E – 21	3.806E – 21
	Mulliken	1.178E – 39	1.18E – 39	1.179E – 39	1.180E – 39
	Deslandres–D'Azambuja	4.564E – 34	3.01E – 34	5.649E – 34	2.757E – 34
	Ballik and Ramsay	6.693E – 20	6.72E – 20	6.534E – 20	6.491E – 20
	Swan	1.513E – 25	1.49E – 25	1.527E – 25	1.540E – 25
	Fox–Herzberg	3.862E – 38	3.84E – 38	3.837E – 38	3.695E – 38
5000	Philips	4.215E – 17	4.58E – 17	4.076E – 17	3.974E – 17
	Mulliken	2.073E – 18	2.11E – 18	2.121E – 18	2.080E – 18
	Deslandres–D'Azambuja	2.824E – 17	1.79E – 17	3.909E – 17	1.723E – 17
	Ballik and Ramsay	7.534E – 17	8.01E – 17	7.106E – 17	6.155E – 17
	Swan	6.947E – 16	6.53E – 16	7.225E – 16	7.045E – 16
	Fox-Herzberg	2.835E – 18	2.69E – 18	2.524E – 18	2.241E – 18
10000	Philips	1.106E – 16	1.60E – 16	1.201E – 16	1.032E – 16
	Mulliken	6.435E – 16	6.59E – 16	6.300E – 16	6.218E – 16
	Deslandres–D'Azambuja	2.527E – 15	1.33E – 15	3.133E – 15	1.459E – 15
	Ballik and Ramsay	1.682E – 16	2.14E – 16	1.590E – 16	1.013E – 16
	Swan	7.462E – 15	7.01E – 15	7.614E – 15	7.358E – 15
	Fox–Herzberg	3.976E – 16	4.18E – 16	3.617E – 16	3.115E – 16

Table 5
Radiative source strength per molecule (W•sr^{-1}•molecule^{-1}) for CO: comparison with the calculated results.

T(K)	Electronic system	This paper	Results from [33]	Results from [41]	Results from [43]
1000	Infrared	5.842E – 21	5.83E – 21	5.797E – 21	5.853E – 21
	Fourth-positive	9.942E – 52	9.89E – 52	1.003E – 51	9.904E – 52
	Hopfield–Birge	7.106E – 67	7.18E – 67	7.218E – 67	7.121E – 67
	Third-positive	1.276E – 64	1.26E – 64	1.283E – 64	
5000	Infrared	1.363E – 19	1.41E – 19	1.383E – 19	1.371E – 19
	Fourth-positive	2.690E – 19	2.75E – 19	2.956E – 19	2.785E – 19
	Hopfield–Birge	1.229E – 23	1.23E – 23	1.231E – 23	4.034E – 23
	Third-positive	7.707E – 23	7.57E – 23	7.973E – 23	1.153E – 22
10000	Infrared	2.951E – 19	3.18E – 19	3.042E – 19	3.009E – 19
	Fourth-positive	2.725E – 15	2.67E – 15	3.299E – 15	2.971E – 15
	Hopfield–Birge	1.394E – 18	1.40E – 18	1.404E – 18	2.264E – 17
	Third-positive	8.840E – 18	8.77E – 18	9.012E – 18	2.297E – 17

given by [1]

$$N_u = N_{total} g \frac{2J+1}{Q_{int}(T_e, T_v, T_r)} exp\left(-\frac{E_{el}(n)}{kT_e} - \frac{E_{vib}(n,v)}{kT_v} - \frac{E_{rot}(n,v,J)}{kT_r}\right) \quad (39)$$

where $Q_{int}(T_e, T_v, T_r)$ is the internal partition function based on the three-temperature model.

In this paper, the Einstein coefficients of the electronic transition systems for diatomic molecules are selected from our previous publication [30]. A Voigt profile is adopted by considering the Doppler broadening calculated at T_r, the collisional broadening calculated at T_r, and the Stark broadening calculated at T_v. Moreover, the calculation of spectral radiative properties for high-temperature equilibrium plasma requires the number densities of all components. For air plasma, the number densities are obtained from Laux et al. [47,59]. Then we calculate the total radiative source strength for air plasma at atmospheric pressure due to the discrete emission of the molecular transition systems. The radiative source strength SR in W cm^{-3} sr^{-1} for the wavenumber range v_1-v_2 is given by [34]

$$SR = \int_{v_1}^{v_2} \kappa_v I_v^0 dv \quad (40)$$

where I_v^0 is the Planck distribution function. The results versus temperature for the wavenumber range 1000–50000 cm^{-1} are calculated and compared with the calculated ones from Ref. [40] and the experimental data from Ref. [59], which are given in Fig. 14. A good agreement is observed for temperatures below 7000 K. Above 7000 K, our results are in good agreement with the calculated ones from Ref. [40], but lower than the experimental data from Ref. [59] since the calculated results in this paper and Ref. [40] do not consider the contribution of atomic components (N and O). For CO_2–N_2 plasma, we calculate the radiative source strength per molecule for CN, C_2, CO and CO^+, respectively. Comparisons with the theoretical results of Refs. [33,41,43] are given in Tables 3–6.

Table 6
Radiative source strength per molecule ($W \bullet sr^{-1} \bullet molecule^{-1}$) for CO^+: comparison with the calculated results.

T(K)	Electronic system	This paper	Results from [33]	Results from [41]	Results from [43]
1000	Comet-tail	3.054E – 27	3.01E – 27	3.077E – 27	3.047E – 27
	Baldet–Johnson	1.632E – 42	1.79E – 42	1.450E – 42	
	First-negative	4.536E – 41	4.15E – 41	4.798E – 41	4.817E – 41
5000	Comet-tail	8.169E – 17	7.96E – 17	8.274E – 17	8.145E – 17
	Baldet–Johnson	1.694E – 19	1.83E – 19	1.528E – 19	1.467E – 19
	First-negative	2.875E – 18	2.67E – 18	3.168E – 18	3.111E – 18
10000	Comet-tail	1.492E – 15	1.54E – 15	1.672E – 15	1.569E – 15
	Baldet–Johnson	1.157E – 16	1.30E – 16	1.240E – 16	1.057E – 16
	First-negative	1.426E – 15	1.34E – 15	1.649E – 15	1.568E – 15

For the most electronic transition systems, discrepancies of lower than 6% have been observed between our calculations and the other results of Refs. [33,41,43]. The Deslandres–D'Azambuja system of C_2 and the Third-positive system of CO are considered the most questionable.

The analysis of the results in Section 4 shows insignificant sensitivity of the partition function and the level energy to the energy partitioning scheme employed. The aim of this section is to study the impact of the two energy partitioning schemes on the spectral radiative properties. Fig. 15 shows the relative spectral radiative intensity of N_2 first and second positive systems (67231 spectral bands), N_2^+ first negative system (2993 spectral bands), CN violet system (14291 spectral bands) and C_2 swan system (1936 spectral bands). The spectral ranges in these figures correspond to vibrational bands characterized by Δv=0. Almost identical results are observed between the spectra calculated using the first energy partitioning scheme and those obtained using the second energy partitioning scheme. And they are both in good agreement with the experimental results measured by da Silva [58], which validate our calculated partition functions and the level energies.

6. Conclusions

In this work, we have presented more accurate high-temperature equilibrium and non-equilibrium partition functions, thermodynamic and spectral radiative properties of N_2, N_2^+, NO, O_2, CN, C_2, CO and CO^+ using an improved calculation of the energy levels. The energy levels were obtained by solving the radial Schrödinger equation over the accurate potential curve. The potential curves of the lower-lying electronic states were reconstructed using RKR inversion procedure based on the most up-to-date spectroscopic constants, and the rest of the potential curves were obtained from the ab-initio results in the literature.

In thermodynamic equilibrium, the partition functions and the specific heats of diatomic molecules considered in this paper are given, in which we found that the electronic excited states play an important role. Compared with the available data in the literature, the partition functions and the specific heats show large sensitivity to the number of electronic states, high-lying level energies and cut-off criterion. The results we obtained are more accurate at high temperatures since more high-lying levels and more precise level energies are considered.

In thermodynamic non-equilibrium, the two-temperature internal partition functions, the average energies and the specific heats of diatomic molecules considered in this paper are given and analyzed for two limiting cases, i.e., the rovibrational interaction energy is assigned fully either to the vibrational contribution or to the rotational contribution. The deviations between the two cases for both the partition functions and the average energies are within 5%. However, for vibrational (rotational) specific heats, larger discrepancies can be observed for high rotational (vibrational) temperature and low vibrational (rotational) temperature due to the effect of splitting the rovibrational interaction energy. In addition, the two-temperature thermodynamic properties can be used for non-equilibrium flow field calculations.

Finally, the radiative source strengths for diatomic molecules of equilibrium air and CO_2–N_2 plasma are calculated, which show discrepancies smaller than 6% with the data in the literature. The spectral radiative intensities for some discrete transitions of N_2, N_2^+, CN and C_2 molecules in thermodynamic nonequilibrium are calculated and validated by available experimental data. The results show that our models can be used to calculate the absorption and emission coefficients for the discrete radiation of high-temperature diatomic gases.

Acknowledgments

This work was supported by the National Natural Science Foundation of China (No.51421063). ZQ sincerely thanks Robert J. Le Roy of university of Waterloo for providing kind guidance of RKR1 code, which is used to calculate the electronic potential curves in this paper.

Appendix A. Selected spectroscopic constants

Tables A1–A9.

Table A1
Correspondence between Dunham coefficients and traditional spectroscopic constants.

	Y_{ij}	i=0	i=1	i=2	i=3	i=4
G_v	j=0	T_e	ω_e	$-\omega_e x_e$	$\omega_e y_e$	$\omega_e z_e$
B_v	j=1	B_e	$-\alpha_e$	γ	δ	η
$-D_v$	j=2	$-D_e$	$-\beta_e$	×	×	×

Table A2
Klein–Dunham coefficients for the selected states[a] of the N_2 molecule (all values are in cm^{-1} except r_e in Angstrom and v_{max}).

	Y_{ij}	i=0	i=1	i=2	D_e	r_e	v_{max}	Ref.
$A'^1\Sigma_u^-$	j=0	68152.7	1530.25	12.075	50181.0	1.2755	6	[24,45]
	j=1	1.4799	1.657E − 2					
	j=2	5.55E − 6						
$W^1\Delta_u$	j=0	72097.4	1559.26	11.63	46237	1.268	21	[24,45]
	j=1	1.498	1.66E − 2					
$^5\Sigma_g^+$	j=0	76436	667		3448	1.55	5	[24,45]
	j=1	0.921						
$g^3\Delta_g$	j=0	87900	742.49	11.85	11209	1.6107	12	[24,45]
	j=1	0.928	1.61E − 2					

[a]Klein–Dunham coefficients for $X^3\Sigma_g^+$, $A^3\Sigma_u^+$, $B^3\Pi_g$, $W^3\Delta_u$, $B'^3\Sigma_u$, $C^3\Pi_u$, $a^1\Pi_g$ can be found in our previous publication [30].

Table A3
Klein–Dunham coefficients for the selected states[a] of the N_2^+ molecule (all values are in cm^{-1} except r_e in Angstrom and v_{max}).

	Y_{ij}	i=0	i=1	i=2	D_e	r_e	v_{max}	Ref.
$a^4\Sigma_u^+$	j=0	25467	2398	14	45901	1.1	5	[24]
	j=1	2.071	1.4E − 2					
$D^2\Pi_g$	j=0	52318.2	911.7	12.606	19204.5	1.48	16	[24]
	j=1	1.113	0.02					

[a]The ab-initio potential curves of $^4\Pi_g$, $^4\Delta_u$, $^4\Sigma_u^-$, $^4\Sigma_g^+$, $^4\Pi_u$, $^4\Delta_g$, $^2\Delta_u$, $^2\Pi_g$, $^2\Sigma_u^-$, $^4\Sigma_g^-$ are directly selected from Ref. [46]. Klein–Dunham coefficients for $X^2\Sigma_g^+$, $A^2\Pi_u$, $B^2\Sigma_u^+$, $C^2\Sigma_u^+$ can be found in our previous publication [30].

Table A4
Klein–Dunham coefficients for the selected states[a] of the NO molecule (all values are in cm^{-1} except r_e in Angstrom and v_{max}).

	Y_{ij}	i=0	i=1	i=2	i=3	D_e	r_e	v_{max}	Ref.
$a^4\Pi$	j=0	38807	1019	12.8		14537	1.415	6	[2]
	j=1	1.1275							
$b^4\Sigma^+$	j=0	47950	1206	15		21184	1.3	4	[2]
	j=1	1.3358							
$L'^2\Phi$	j=0	53637	1004.4	11		18932	1.415	4	[48]
	j=1	1.1275							
$F^2\Delta$	j=0	61800	2394	20		10769	1.067	4	[24]
	j=1	1.982	2.3E − 2						
$H^2\Sigma^+$	j=0	62473.4	2339.4			10096	1.061	4	[24]
	j=1	2.003	1.8E − 2						
$H'^2\Sigma^+$	j=0	62485.4	2371.3	16.17		86936	1.0585	12	[24]
	j=1	2.015	2.1E − 2						
$G^2\Sigma^-$	j=0	62913	1085.54	11.083	−0.144	9656	1.3427	4	[24]
	j=1	1.2523	2.04E − 2						
$L^2\Pi$	j=0	63040	952	11.28		19144	1.412	8	[48]
	j=1	1.132	2.21E − 2						
$K^2\Pi$	j=0	64077.5	2438.3	48.38		18106	1.0535	7	[48]
	j=1	2.034	5.6E − 2						

[a]Klein–Dunham coefficients for $X^2\Pi_r$, $A^2\Sigma^+$, $B^2\Pi_r$, $C^2\Pi_r$, $D^2\Sigma^+$, $B'^2\Delta$, $E^2\Sigma^+$ can be found in our previous publication [30].

Table A5
Klein–Dunham coefficients for the selected states[a] of the O_2 molecule (all values are in cm^{-1} except r_e in Angstrom and v_{max}).

	Y_{ij}	i=0	i=1	i=2	i=3	i=4	D_e	r_e	v_{max}	Ref.
$a^1\Delta_g$	j=0	7918.1	1483.5	12.9			34130	1.21563	15	[24]
	j=1	1.4264	1.71E − 2							
	j=2	4.86E − 6								
$b^1\Sigma_g^+$	j=0	13195.1	1432.77	14			28852.9	1.22688	12	[24]
	j=1	1.40037	1.82E − 2							
	j=2	5.351E − 6								
$c^1\Sigma_u^-$	j=0	33057.3	794.29	12.736	−0.244	5E − 4	8991	1.5174	10	[24]
	j=1	0.915	1.39E − 2							
	j=2	7.4E − 6								
$C^3\Delta_u$	j=0	34690	850	20			7358	1.48	6	[24]
	j=1	0.96	2.6E − 2							
$A^3\Sigma_u^+$	j=0	35397.8	799.07	12.16	−0.55		6651	1.5215	4	[24]
	j=1	0.9106	1.41E − 2	−9.7e − 4						
	j=2	4.7e − 6								
$D^3\Sigma_u^+$	j=0	75260	1957	19.7			22101	1.104	3	[24]
	j=1	1.73	2.5E − 2							
$f^1\Sigma_u^+$	j=0	76091	1927	19			21270	1.113	3	[24]
	j=1	1.703	−2E − 2							
$E^2\Sigma_u^-$	j=0	79883	2547				17478	1.2	4	[24]
	j=1	1.4638								

[a]The ab-initio potential curves of $^5\Pi$, $2^3\Sigma_g^+$, $2^3\Pi_g$, $3^3\Pi_g$, $^1\Pi_g$, $^3\Pi_g$, $^1\Delta_u$, $^3\Delta_u$, $2^1\Delta_g$, $^1\Phi_g$, $^1\Sigma_u^+$ are directly selected from Ref. [49]. Klein–Dunham coefficients for $X^3\Sigma_g^-$, $B^3\Sigma_u^-$ can be found in our previous publication [30].

Table A6
Klein–Dunham coefficients for the selected states[a] of the CN molecule (all values are in cm^{-1} except r_e in Angstrom and v_{max}).

	Y_{ij}	i=0	i=1	i=2	i=3	D_e	r_e	v_{max}	Ref.
$J^2\Delta_i$	j=0	65258.19	1121.76	14.203	0.18	9428.5	1.457	4	[24]
	j=1	1.305	2.08E − 2						
	j=2	5.8E − 6							

[a]The ab-initio potential curves of $b^4\Pi$, $c^4\Delta$, $d^4\Sigma^-$, $H^2\Pi_r$, $G^2\Phi$, $^2\Sigma^-$, $^4\Delta$, $^2\Sigma^-$II are directly selected from Ref. [50]. And the ab-initio potential curves of $a^4\Sigma^+$, $D^2\Pi_i$, $1^2\Sigma^-$, $E^2\Sigma^+$, $F^2\Delta_r$ are directly selected from Ref. [51]. Klein–Dunham coefficients for $X^2\Sigma^+$, $A^2\Pi_i$, $B^2\Sigma^+$can be found in our previous publication [30].

Table A7
Klein–Dunham coefficients for the selected states[a] of the C_2 molecule (all values are in cm^{-1} except r_e in Angstrom and v_{max}).

	Y_{ij}	i=0	i=1	i=2	i=3	D_e	r_e	v_{max}	Ref.
$^5\Pi_g$	j=0	22485	1400			28552.01	1.46	10	[52]
	j=1	1.8							
$^5\Sigma_g^+$	j=0	30474	1550			20567	1.35	6	[52]
	j=1	1.8							
$C'^1\Pi_g$	j=0	39365	1697			10565.8	1.3013	3	[53]
	j=1	1.7113	4.3E − 2						
	j=2	1.13E − 5							
$E^1\Sigma_g^+$	j=0	55034.7	1671.5	40.02	0.248	16861.2	1.2529	4	[24]
	j=1	1.793	4.21E − 2	−5e − 4					
	j=2	8.3E − 6	6E − 7						
$f^3\Sigma_g^-$	j=0	71045.8	1360.5	14.8		39535.55	1.399	3	[24]
	j=1	1.448	0.4						
	j=2	10e − 6							
$g^3\Delta_g$	j=0	73183.6	1458.06			37535.55	1.3579	5	[24]
	j=1	1.5238	1.7E − 2						
	j=2	6.6E − 6							
$F^1\Pi_u$	j=0	75456.9	1557.5			35124.45	1.307	4	[24]
	j=1	1.645	1.9E − 2						

[a]The ab-initio potential curves of $B^1\Delta_g$, $B'^1\Sigma_g^+$ are directly selected from Ref. [45]. And the potential curves of $C^2\Pi_g$, $^1\Sigma_u^-$, $^3\Delta_u$ are directly selected from Ref. [54]. Klein–Dunham coefficients for $X^1\Sigma_g^+$, $a^3\Pi_u$, $b^3\Sigma_g^-$, $A^1\Pi_u$, $c^3\Sigma_u^+$, $d^3\Pi_g$, $e^3\Pi_g$, $D^1\Sigma_g^+$ can be found in our previous publication [30].

Table A8
Klein–Dunham coefficients for the selected states[a] of the CO molecule (all values are in cm^{-1} except r_e in Angstrom and v_{max}).

	Y_{ij}	i=0	i=1	i=2	D_e	r_e	v_{max}	Ref.
$^5\Pi$	j=0	62507.5	759	25.2	3548.81	1.78	5	[55]
	j=1	0.931	0.0231					

[a]The ab-initio potential curves of $e^3\Sigma^-$, $I^1\Sigma^-$, $D^1\Delta$ are directly selected from Ref. [56]. Klein–Dunham coefficients for $X^1\Sigma^+$, $a^3\Pi_r$, $a'^3\Sigma^+$, $d^3\Delta_i$, $A^1\Pi$, $B^1\Sigma^+$, $b^3\Sigma^+$ can be found in our previous publication [30].

Table A9
Klein–Dunham coefficients for the selected states[a] of the CO^+ molecule (all values are in cm^{-1} except r_e in Angstrom and v_{max}).

	Y_{ij}	i=0	i=1	i=2	D_e	r_e	v_{max}	Ref.
$C^2\Delta$	j=0	63012	1144	33.3	5626.7	1.396	4	[55]
	j=1	1.357	0.024					

[a]The ab-initio potential curves of $a^4\Sigma^+$, $^4\Delta$, $b^4\Pi$, $^4\Sigma$ are directly selected from Ref. [42,57]. Klein–Dunham coefficients for $X^2\Sigma^+$, $A^2\Pi_i$, $B^2\Sigma^+$ can be found in our previous publication [30].

References

[1] Burn R. High temperature phenomena in shock waves. Berlin Heidelberg: Berlin: Springer-Verlag; 2012.
[2] Babou Y, Rivière P, Perrin MY, Soufiani A. High-temperature and non-equilibrium partition function and thermodynamic data of diatomic molecules. Int J Thermophys 2009;30(2):416–38.
[3] Mihalas D. Stellar atmospheres. San Francisco: Freeman and Company; 1970.
[4] Chauveau S, Deron C, Perrin MY, Rivière P, Soufiani A. Radiative transfer in LTE air plasmas for temperatures up to 15,000K. J Quant Spectrosc Radiat Transf 2003;77(2):113–30.
[5] Jaffe RL. The calculation of high-temperature equilibrium and non-equilibrium specific heat data for N_2, O_2 and NO. AIAA 22nd thermophysics conference; 1987.
[6] Giordano D, Capitelli M, Colonna G. Tables of internal partition functions and thermodynamic properties of high-temperature air species from 50K to 100000K. ESA Sci Tech Rev 1994;246(5):471–8.
[7] Capitelli M, Colonna G, Giordano D, Marraffa L, Casavola V, Minelli P, Pagano D, Pietanza LD, Taccogna F, Warmbein B. Tables of internal partition functions and thermodynamic properties of high-temperature Mars-atmosphere species from 50K to 50000K. ESA Sci Tech Rev 2005;246:1–267.
[8] Pagano D, Casavola A, Pietanza L D, Capitelli M, Colonna G, Giordano D, Marraffa L. Internal partition functions and thermodynamic properties of high--temperature Jupiter-atmosphere species from 50K to 50,000K. ESA Sci Tech Rev 2009;257:1–86.
[9] Lee JH. Basic governing equations for the flight regimes of aeroassisted orbital transfer vehicles. AIAA Prog Astronautics Aeronaut Therm Des Aeroassisted Transfer Veh 1985;96:3–53.
[10] Park C. Assessment of a two-temperature kinetic model for dissociating and weakly ionizing nitrogen. J Thermophys Heat Transfer 1988;2(1):8–16.
[11] Panesi M, Munafò A, Magin T E, Jaffe R L. Non-equilibrium shock-heated nitrogen flows using a rovibrational state-to-state method. Phys Rev E 2014;90(1):013009.
[12] Lopez B, da Silva ML. SPARK: a software package for aerodynamics, radiation and kinetics. In: 46th AIAA thermophysics conference; 2016. p. 4025.
[13] Bonelli F, Tuttafesta M, Colonna G, Cutrone L, Pascazio G. An MPI-CUDA approach for hypersonic flows with detailed state-to-state air kinetics using a GPU cluster. Comput Phys Commun 2017;219:178–95.
[14] Drellishak KS, Knopp CF, Cambel AB. Partition functions and thermodynamic properties of argon plasma. Phys Fluids 1963;6(9):1280–8.
[15] Drellishak KS, Aeschliman DP, Cambel AB. Partition functions and thermodynamic properties of nitrogen and oxygen plasmas. Phys Fluids 1965;8(9):1590–600.
[16] McBride BJ, Zehe MJ, Gordon S. NASA Glenn coefficients for calculating thermodynamic properties of individual species. NASA; 2002. Tech. Paper 2002-211556.
[17] Herzberg G. Molecular spectra and molecular structure: spectra of diatomic molecules. New York: Van Nostrand Reinhold Company; 1950.
[18] da Silva ML, Guerra V, Loureiro J, Sá PA. Vibrational distributions in N_2 with an improved calculation of energy levels using the RKR method. Chem Phys 2008;348(1):187–94.
[19] Rydberg R. Graphische darstellung einiger bandenspektroskopischer ergebnisse. Z Phys 1932;73(5-6):376–85.
[20] Klein O. Zur berechnung von potentialkurven für zweiatomige moleküle mit hilfe von spektraltermen. Z Phys 1932;76(3):226–35.
[21] Rees ALG. The calculation of potential-energy curves from band-spectroscopic data. Proc Phys Soc 1947;59(6):998.
[22] Laurendeau NM. Statistical thermodynamics: fundamentals and applications. England: Cambridge University Press; 2005.
[23] Huang K. Statistical mechanics. Phys Today 1965;18(1) 92--92.
[24] Huber KP, Herzberg G. Molecular spectra and molecular structure: constants of diatomic molecules. New York: D. Van Nostrand Reinhold Company; 1979.
[25] Roy RJL, Huang Y, Jary C. An accurate analytic potential function for ground-state N_2 from a direct-potential-fit analysis of spectroscopic data. J Chem Phys 2006;125(16):164310.
[26] Zhang X, Zhai H, Liu S, Liu Y. Extensive theoretical study on the excited states of the PCl^+ molecule including spin-orbit coupling. J Quant Spectrosc Radiat Transfer 2017;196:142–8.
[27] Elmoussaoui S, Chmaisani W, Korek M. Theoretical electronic structure with dipole moment and rovibrational calculation of the low-lying electronic states of the HgF molecule. J Quant Spectrosc Radiat Transfer 2017;201:64–74.
[28] Herzberg G. Molecular spectra and molecular structure I. Spectra of diatomic molecules. New York: D. Van Nostrand; 1950.
[29] Le Roy RJ. RKR1: a computer program implementing the first-order RKR method for determining diatomic molecule potential energy functions. J Quant Spectrosc Radiat Transfer 2017;186:158–66.
[30] Qin Z, Zhao JM, Liu LH. Radiative transition probabilities for the main diatomic electronic systems of N_2, NO, O_2, CO, CO^+, CN, C_2 and H_2 produced in plasma of atmospheric entry. J Quant Spectrosc Radiat Transfer 2017;202:286–301.
[31] Kauzmann W. Quantum chemistry. New York: Academic Press; 1957.
[32] Jensen F. Introduction to computational chemistry. UK: John wiley & sons; 2017.
[33] Billoux T, Cressault Y, Gleizes A. Net emission coefficient for CO–H_2 thermal plasmas with the consideration of molecular systems. J Quant Spectrosc Radiat Transfer 2015;166:42–54.
[34] Babou Y, Rivière P, Perrin MY, Soufiani A. Spectroscopic study of microwave plasmas of CO_2 and CO_2–N_2 mixtures at atmospheric pressure. Plasma Sources Sci Technol 2008;17(4):045010.
[35] Lamet JM, Babou Y, Riviere P, Soufiani A. Radiative transfer in gases under thermal and chemical non-equilibrium conditions: application to earth atmospheric re-entry. J Quant Spectrosc Radiat Transfer 2008;109(2):235–44.
[36] Hulburt HM, Hirschfelder JO. Potential energy functions for diatomic molecules. J Chem Phys 1941;9(1):61–9.
[37] Billoux T, Cressault Y, Gleizes A. Tables of radiative transition probabilities for the main diatomic molecular systems of OH, CH, CH^+, CO and CO^+ occurring in CO-H_2 syngas-type plasma. J Quant Spectrosc Radiat Transfer 2014;133:434–44.
[38] Balint-Kurti GG, Dixon RN, Marston CC. Grid methods for solving the Schrödinger equation and time dependent quantum dynamics of molecular photofragmentation and reactive scattering processes. Int Rev Phys Chem 1992;11(2):317–44.
[39] Marston CC, Balint-Kurti GG. The Fourier grid Hamiltonian method for bound state eigenvalues and eigenfunctions. J Chem Phys 1989;91(6):3571–6.
[40] Chauveau S, Perrin MY, Rivière P, Soufiani A. Contributions of diatomic molecular electronic systems to heated air radiation. J Quant Spectrosc Radiat Transfer 2002;72(4):503–30.
[41] Babou Y, Rivière P, Perrin MY, Soufiani A. Spectroscopic data for the prediction of radiative transfer in CO_2–N_2 plasmas. J Quant Spectrosc Radiat Transfer 2009;110(1-2):89–108.
[42] Okada K, Iwata S. Accurate potential energy and transition dipole moment curves for several electronic states of CO^+. J Chem Phys 2000;112(4):1804–8.
[43] Kuznetsova L, Surzhikov S. Absorption cross sections of diatomic molecules for problems or radiative heat transfer in low temperature plasmas. High Temp 1999;37:374–85.
[44] Panesi M. Physical models for non-equilibrium plasma flow simulations at high speed reentry conditions PhD thesis. Belgium: von Karman Institute for Fluid Dynamics, Rhode-St-Genése; 2009.
[45] Jiang W, Wilson AK. Multireference composite approaches for the accurate study of ground and excited electronic states: C_2, N_2, and O_2. J Chem Phys 2011;134(3):034101.
[46] Thulstrup EW, Andersen A. Configuration interaction studies of bound, low-lying states of N_2^-, N_2, N_2^+ and N_2^{++}. J Phys B-At Mol Opt Phys 1975;8(6):965.
[47] Laux CO, Spence TG, Kruger CH, Zare RN. Optical diagnostics of atmospheric pressure air plasmas. Plasma Sources Sci Technol 2003;12(2):125–38.
[48] Gallusser R, Dressler K. Multistate vibronic coupling between the excited $^2\Pi$ states of the NO molecule. J Chem Phys 1982;76(9):4311–27.
[49] Liu H, Shi D, Sun J, Zhu Z, Zhang S. Accurate calculations on the 22 electronic states and 54 spin-orbit states of the O_2 molecule: Potential energy curves, spectroscopic parameters and spin-orbit coupling. Spectroc Acta Pt A–Mol Biomol Spectr 2014;124:216–29.
[50] Schaefer HF, Heil TG. Electronic Structures and potential energy curves for the low-lying states of the CN radical. J Chem Phys 1971;54(6):2573–80.
[51] Shi D, Li W, Sun J, Zhu Z. MRCI study on spectroscopic and molecular properties of several low-lying electronic states of the CN radical. J Quant Spectrosc Radiat Transfer 2011;112(14):2335–46.
[52] Fougere PF, Nesbet RK. Electronic structure of C_2. J Chem Phys 1966;44(1):285–98.
[53] Messerle G, Krauss L. Ein neues $c'^1\Pi_g$—$b^1\Pi_u$-Bandensystem des C_2-Moleküls. Zeitschrift für Naturforschung A 1967;22(12):2015–23.
[54] Boggio-Pasqua M, Voronin AI, Halvick P, Rayez J-C. Analytical representations of high level ab initio potential energy curves of the C_2 molecule. J Mol Struct 2000;531(1):159–67.
[55] O'Neil SV, Schaefer HF. Valence-excited states of carbon monoxide. J Chem Phys 1970;53(10):3994–4004.

[56] Shi DH, Li WT, Sun JF, Zhu ZL. Theoretical study of spectroscopic and molecular properties of several low-lying electronic states of CO molecule. Int J Quantum Chem 2013;113(7):934–42.
[57] Shi D, Li W, Sun J, Zhu Z, Liu Y. MRCI study of potential energy curves, spectroscopic and molecular properties of the CO^+ cation. Comput Theor Chem 2011;978(1):126–37.
[58] Lino da Silva M. Simulation des propriétés radiatives du plasmaentourant un véhicule traversant une atmosphère planétaire àvitesse hypersonique - application à la planète Mars. Université d'Orléans; 2004.
[59] Laux CO. Optical diagnostics and radiative emission of air plasma PhD Thesis. Stanford University; 1993.